AGU ADVANCING EARTH AND SPACE SCIENCES

Paleoceanography and Paleoclimatology

RESEARCH ARTICLE
10.1029/2024PA004976

Impact of Model Tuning on Simulated Mid-Pliocene Warming

Xin Ren[1], Paul Valdes[1], Daniel J. Lunt[1], Alan M. Haywood[2], Erica Hendy[3], Julia C. Tindall[2], Phoebe Ross[4], and Sebastian Steinig[1]

[1]School of Geographical Sciences, University of Bristol, Bristol, UK, [2]School of Earth and Environment, University of Leeds, Leeds, UK, [3]School of Earth Sciences, University of Bristol, Bristol, UK, [4]Department of Earth Science and Engineering, Imperial College London, London, UK

Key Points:

- HadCM3t aligns better with the reconstructed sea surface temperature anomalies for the mid-Pliocene simulation than the original HadCM3
- HadCM3t produces higher warming in mid to high latitudes, driven by changes in emissivity and surface albedo
- Shortwave radiation changes contributing to the larger warming in HadCM3t than HadCM3 mainly result from surface albedo and cloud variations

Supporting Information:

Supporting Information may be found in the online version of this article.

Correspondence to:

X. Ren,
xinxin.ren@bristol.ac.uk

Citation:

Ren, X., Valdes, P., Lunt, D. J., Haywood, A. M., Hendy, E., Tindall, J. C., et al. (2025). Impact of model tuning on simulated Mid-Pliocene warming. *Paleoceanography and Paleoclimatology*, *40*, e2024PA004976. https://doi.org/10.1029/2024PA004976

Received 24 JUL 2024
Accepted 11 APR 2025

Author Contributions:

Conceptualization: Xin Ren, Paul Valdes, Daniel J. Lunt
Data curation: Alan M. Haywood, Julia C. Tindall
Formal analysis: Xin Ren
Funding acquisition: Daniel J. Lunt, Erica Hendy
Methodology: Paul Valdes, Daniel J. Lunt, Alan M. Haywood, Julia C. Tindall, Phoebe Ross, Sebastian Steinig
Project administration: Daniel J. Lunt, Erica Hendy
Software: Sebastian Steinig
Supervision: Daniel J. Lunt, Erica Hendy
Writing – original draft: Xin Ren

Abstract A tuned version of HadCM3 (HadCM3t) is used to simulate the climate of the mid-Pliocene warm period (mPWP) and is compared with the original untuned version of HadCM3 (HadCM3u). After the tuning, HadCM3t performs as well as HadCM3u in simulating the preindustrial climate, but aligns better with the reconstructed mPWP sea surface temperature anomalies, primarily due to a better representation of high latitude warming. Regarding the mPWP climate anomaly relative to the preindustrial, compared to HadCM3u, HadCM3t produces stronger mid-to-high latitude warming with polar warming 2.2 times the global mean, which is higher than the 2.0 of HadCM3u. The warming of the mPWP is primarily explained by an increase in emissivity and surface albedo. The warming of the polar regions induced by emissivity and surface albedo from HadCM3t is higher by 0.6°C and 0.7°C respectively, than that from HadCM3u, leading to warmer mPWP high latitudes. The increase in shortwave radiation over the Polar Regions is driven mainly by changes in surface albedo, which lead to a temperature rise of +0.7°C, and by changes in cloud cover, which contribute an additional +0.1°C to the temperature increase. Here, the increased cloud-induced shortwave radiation change is due to decreased cloud fraction and decreased cloud scattering effect; the increased surface albedo-induced radiative effects result from the increased ice loss due to warm high latitudes. This tuning allows models like HadCM3 to better align with proxy data, offering a more reliable baseline for projecting future scenarios under similar conditions.

Plain Language Summary A tuned version of the HadCM3 model (HadCM3t) is utilized to study the climate of the mid-Pliocene warm period. Compared to the original HadCM3, the simulations produced by HadCM3t align better with the reconstructed sea surface temperature anomalies, primarily due to an improved representation of high-latitude warming. This improvement is attributed to the additional warming induced by changes in emissivity and surface albedo over high latitudes. Further analysis reveals that variations in cloud cover also make contributions to the additional polar warming due to changes in both shortwave and longwave radiation. This study underscores the value of using past climate data to refine model parameters, which provides insights for improving model performance in simulating future climate with similar conditions and feedback mechanisms.

1. Introduction

1.1. The Mid-Pliocene and PlioMIP

The mid-Pliocene warm period (mPWP; or the mid Piacenzian) was an interval around 3.3 to 3 million years before present (Ma) that was characterized by atmospheric CO_2 concentrations of around 400 ppm, with warmer temperatures and modified geography compared to present (e.g., Haywood et al., 2020). The mPWP has been broadly studied in terms of proxy reconstruction (e.g., Dowsett et al., 2016; McClymont et al., 2020, 2023) and climate simulations in the Pliocene Model Intercomparison Project (PlioMIP; e.g., Haywood et al., 2013, 2020, 2024).

Comparison between the proxy reconstructions and model results helps validate models. Although PlioMIP2 made improvement on reducing model-data discrepancy seen in PlioMIP1, disagreement still exists (Tindall et al., 2022). Comparing with proxy reconstructions, most PlioMIP2 models produced a relatively lower global mean sea surface temperatures (SST) warmings (McClymont et al., 2020). Specifically, models underestimate the warming in the south-west off the coast area of Africa, the Mediterranean Sea, one site off the east coast of North

Writing – review & editing: Xin Ren, Daniel J. Lunt, Erica Hendy, Julia C. Tindall, Phoebe Ross

America, and one site at the west of Svalbard, relative to proxy reconstructions (details are shown in Figure 8 of Haywood et al. (2020) and Figure 1 of Tindall et al. (2022)). There are three possible contributors to model-data disagreement: boundary condition uncertainty, data uncertainty and modeling uncertainty (Haywood et al., 2016). From a modeling perspective, there are 3 ways to improve model-data agreement: (a). Reducing the uncertainties in the boundary conditions, such as conducting sensitivity studies that vary insolation, CO_2 concentration, topography, etc (e.g., Feng et al., 2017; Hill, 2015; Howell et al., 2016); (b). Reducing structural uncertainties in models, such as studies that investigated and sampled models' structural uncertainties (e.g., Dolan et al., 2018; Haywood et al., 2016; Tindall et al., 2022); (c). Reducing parameter uncertainties in models, such as in Feng et al. (2019), which examined the importance of parameterization of aerosol-cloud interactions for the mPWP simulation. However, structural uncertainty exists in all models to some extent. Therefore, this study focuses on reducing parameter uncertainties through model tuning.

1.2. Model Tuning

Model tuning is an important process in climate model development. By taking the parametric uncertainty of specific variables into consideration, the model can be tuned to better represent observations. A survey conducted by Hourdin et al. (2017) showed that the most commonly adjusted properties are cloud and surface albedo related uncertainties to achieve an equilibrium global net top-of-atmosphere flux and global-mean surface temperature closer to observations. In one widely used approach (Perturbed Parameter Ensembles, PPE) poorly constrained parameters, that represent specific subgrid-scale processes in a single model, are perturbed to produce an ensemble of model members (J. M. Murphy et al., 2004). This approach allows precise investigation of possible parameter combinations based on the plausible range of uncertain parameters in one model (Irvine et al., 2013). The PPE approach has been used in climate projections such as the 2009 UK Climate Projections (UKCP09) (J. Murphy et al., 2009), and to tune models such as the Hadley Center Climate Model (HadCM3) (Irvine et al., 2013; Mulholland et al., 2017; Roach et al., 2018), HadGEM3 (Sexton et al., 2021; Yamazaki et al., 2021), and other models (e.g., Gregoire et al., 2011; Peatier et al., 2022; Shiogama et al., 2012). This approach has been used to address the problem of models becoming unstable at high CO2 concentrations (e.g., J. M. Murphy et al., 2004; Sanderson, 2011; Shiogama et al., 2014), and to address the long-standing equable climate problem that involves model-data disagreement in high latitude temperatures during warm periods, such as the Eocene (Ross, 2023; Sagoo et al., 2013). Therefore, it is practical to apply model tuning to HadCM3 in simulating the mPWP.

1.3. HadCM3 in PlioMIP

The Hadley Center Climate Model (HadCM3) is a fully coupled atmosphere-ocean general circulation model which has been widely used in studies of climate prediction, past climate simulation, and climate detection and attribution. For example, HadCM3 is one of the major models used in scientific projects such as the IPCC Third and Fourth Assessments (Houghton et al., 2001; Solomon et al., 2007), UK Climate Projections, and the Met Office decadal prediction system (Smith et al., 2007). It is particularly useful in paleoclimate investigations that require long runs, such as the Paleoclimate Modeling Intercomparison Project. Descendants of HadCM3 (HadGEM2 and HadGEM3) have also participated in PlioMIP (Tindall & Haywood, 2020; Williams et al., 2021). Both HadGEM3 and HadGEM2 show a greater extent of polar amplification than HadCM3, due to the high latitude warming, both show higher agreement with proxy reconstructed SST anomalies (SSTA) than HadCM3 (Tindall & Haywood, 2020; Williams et al., 2021). Nevertheless, HadCM3 is still widely used in paleoclimate simulations due to its high computational efficiency and good performance in long simulations (Valdes et al., 2017). For example, HadCM3 is more than 1,000 times faster than some complex versions of the UK Met Office Unified Model (Valdes et al., 2017), 20 times faster than HadGEM2 (Tindall & Haywood, 2020), and the computational needs in terms of core hours for HadGEM3 are about 1,000 times (20 times slower with 50 times more CPUs) larger than for HadCM3. Therefore, it is a useful exercise to attempt to improve the match between SSTA produced by HadCM3 and proxy reconstructions, in particular the underestimation of warming over high latitudes.

Two versions of HadCM3 that use different land surface schemes—the Met Office Surface Exchange scheme version 1 (MOSES1) and MOSES2, participated in PlioMIP Phase 1 (Bragg et al., 2012) and Phase 2 (Hunter et al., 2019). In response to CO_2 concentrations of 400 ppm, and prescribed mPWP boundary conditions including topography, orbital configuration, solar insolation, HadCM3 in PlioMIP2 produced a 2.9°C warmer mPWP than the preindustrial and a polar amplification factor (the ratio of warming poleward of 60°N and 60°S to the global

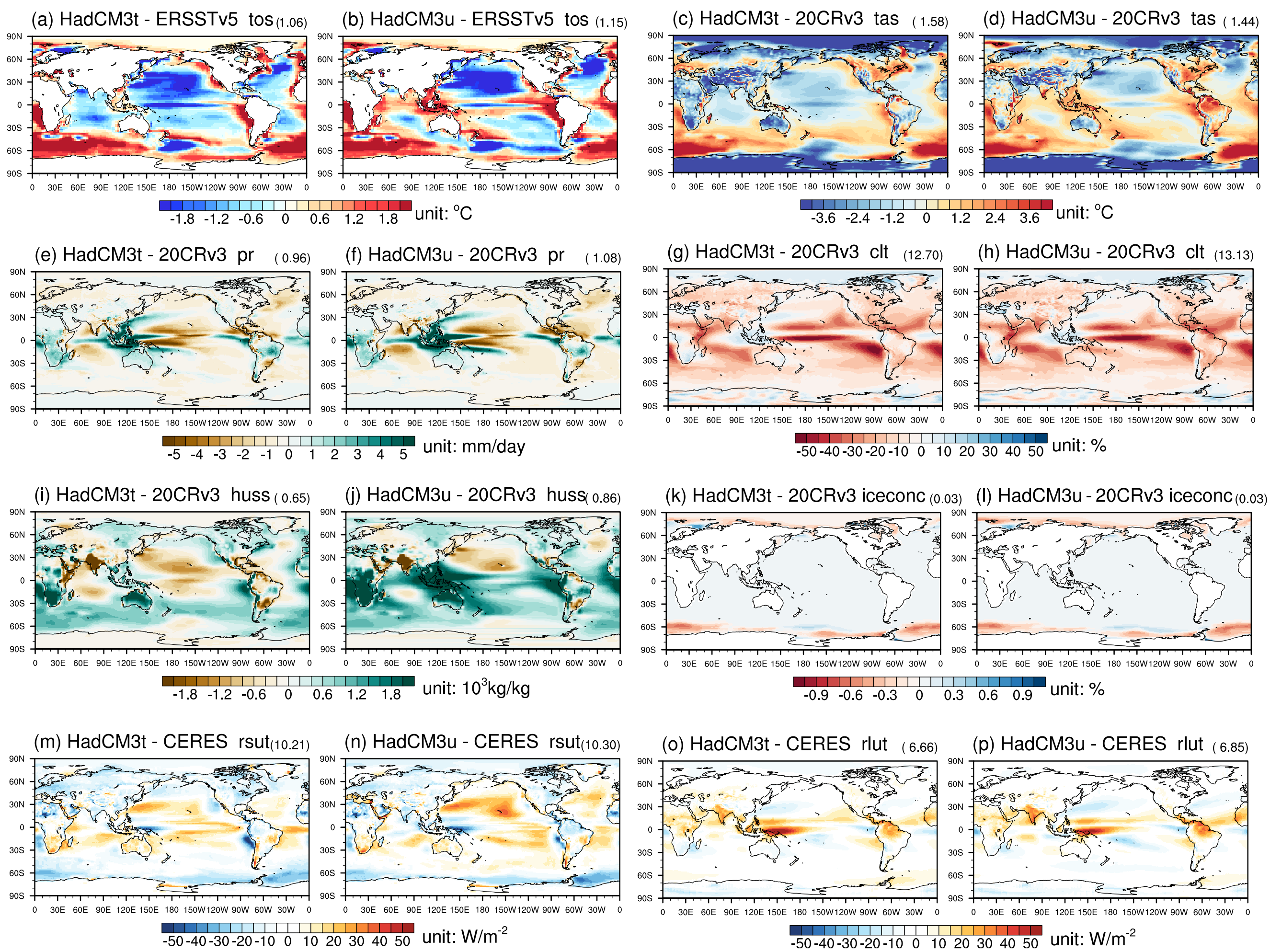

Figure 1. Comparison of simulated PI climate from HadCM3t and HadCM3u with reanalysis data. (a, b) SST; (c, d): surface air temperature (tas); (e, f): precipitation (pr); (g, h): cloud coverage (CLT); (i, j): surface specific humidity (HUSS); (k, l): ice concentration; (m, n): the top-of-atmosphere (TOA) upwelling shortwave (RSUT); (o, p): TOA upwelling longwave (RLUT). The number on the right top of each figure is the root mean squared error between simulated PI and reanalysis data for each variable. A Taylor diagram of this comparison is as shown in Figure S6 in Supporting Information S1.

mean warming (Smith et al., 2019)) of 1.7–2.2 (Hunter et al., 2019). HadCM3 with MOSES1 in PlioMIP1 produced a slightly higher global mean warming of 3.3°C in the mPWP than the preindustrial and a polar amplification factor of 1.9, as calculated from the simulations of Bragg et al. (2012). Note that PlioMIP1 and PlioMIP2 have different boundary conditions as well as different versions of HadCM3 involved. In PlioMIP2, The discrepancies between HadCM3 and proxy reconstructions are similar to that from other models (Haywood et al., 2020). Quantitatively speaking, HadCM3 performed well in terms of reproducing preindustrial SST and SST anomalies (SSTA) in the mPWP compared with the preindustrial (Ren et al., 2023).

1.4. Research Questions

In this paper, we explore a newly tuned version of HadCM3 and aim to solve the following scientific questions:

(1) What changes are produced by parameter tuning (i.e., what is the difference between the tuned HadCM3 (HadCM3t) and untuned HadCM3 (HadCM3u) in simulating the mPWP climatology anomalies)?
(2) Does the tuned version of HadCM3 perform better in simulating mPWP climatology, when compared with reconstructions?
(3) What physical processes contribute to the mPWP temperature anomaly differences between the HadCM3t and HadCM3u?

Sections 2.1 and 2.2 of this paper describe the design of experiments and tuned parameters implemented into the tuned version of HadCM3 (HadCM3t), Section 2.3 shows the approaches used in this study to decompose the Earth's energy imbalance into different components (i.e., an one-dimensional energy balance model (EBM) and the approximate partial radiative perturbation (APRP) method (APRP)), followed by the experiments' spin-up. In Section 3.1, we first compare HadCM3t and the original version of HadCM3 (HadCM3t) simulated preindustrial (PI) climate with observations. Then in Sections 3.2 the SSTAs of the mPWP relative to PI produced by HadCM3t and HadCM3u are described and compared with reconstructed SSTAs. Section 3.3 describes other climatology anomalies in addition to SSTA, and Section 3.4 and 3.5 show the energy balance analyses of the mPWP relative to PI from HadCM3t and HadCM3u using the two approaches. In the discussion Section 4.1, we compare the tuned HadCM3 with other PlioMIP2 models and quantify the similarity and discrepancy between them. In Section 4.2, we discuss the effect of model tuning on simulated mPWP and PI climate. In Section 4.3, we put the results of two energy budget analyses (EBM and APRP) together and then discuss the effects of individual tuned parameters on the mPWP and the PI simulations. Conclusions are presented in Section 5.

2. Methodology

This section describes the methodology used in this paper. First, the HadCM3 model and the experimental design are described briefly. Second, the parameters tuned in the HadCM3 are presented. Third, the energy balance analysis approaches adopted in this paper are described. Finally, the spin-up of simulations are shown.

2.1. HadCM3 and Experimental Design

The model adopted in this paper is HadCM3, which is a fully coupled atmosphere-ocean general circulation model developed in 1999 by the UK Hadley Center (Gordon et al., 2000). In this study, the untuned version of HadCM3 is more formally known as HadCM3B-M2.1aN (Valdes et al., 2017), which is a version derived and developed from the original UK Met Office HadCM3 (Gordon et al., 2000; Pope et al., 2000). Some adaptions were made to the original Met Office version to make it suitable for long-term paleoclimate simulation, for example, changing the land surface scheme from MOSES (Met Office Surface Exchange Scheme) version 1 to version 2.1a; for a detailed description of the adaptions made, see Valdes et al. (2017) and Lunt et al. (2021). Here, B denotes Bristol; M2.1a denotes the MOSES2.1a land surface exchange scheme (Cox et al., 1999); N denotes no change in vegetation (i.e., static prescribed vegetation distribution). The model uses a Cartesian grid, with horizontal resolution of 2.5°× 3.75° (73 × 96 grid boxes; latitude × longitude) in the atmosphere, which has 19 layers vertical levels; this is about 420 km × 280 km at the Equator, reducing to 300 × 280 km at 45° of latitude. For the oceanic component, the resolution is 1.25°× 1.25° with 20 vertical levels (Gordon et al., 2000; Johns et al., 1997; Pope et al., 2000). In this paper, we refer to the untuned version of HadCM3B-M2.1a(N) as HadCM3u and the tuned version as HadCM3t.

In this study, we adopt the pre-industrial (PI) and the mPWP experiment designs following the PlioMIP2 project (Haywood et al., 2016). The PI is the control experiment for the preindustrial with modern boundary conditions, including topography, ice sheets, soil, vegetation, lakes, land-sea mask and a concentration of 280 ppm of CO_2 in the atmosphere. The mPWP is the experiment simulating the mid-Piacenzian warm period during the Pliocene, forced with all Pliocene boundary conditions. More details of the experimental design are described in Haywood et al. (2016). The vegetation scheme used in MOSES2.1a is represented with nine surface types including five plant functional types (broadleaf tree, needleleaf tree, C3 grass, C4 grass, and shrub), soil (desert), urban, water (lake) and ice for the mPWP and PI, which are shown in Figure S1 in Supporting Information S1. Both the mPWP experiments of HadCM3t and HadCM3u are initialized from the last model year of the PlioMIP2 Pliocene core experiment of the untuned HadCM3 Hunter et al., 2019; the PI experiments of HadCM3t and HadCM3u are initialized from the last model year of the PlioMIP2 PI experiment of the untuned HadCM3 conducted by Hunter et al. (2019).

2.2. Perturbed Parameters

Table 1 shows details of the parameter tuning implemented in HadCM3t as used in this paper. Model tuning used in this paper follows similar process for HadCM3BL-M2.1N in Ross (2023) which divide these processes into three parts based on the targets and approaches: "objective," "subjective" and "process-improvement."

Table 1
List of Model Parameters Tuned According to Table 3.1 and Table 3.2 From Ross (2023), Giving the Values Before and After Tuning, and Brief Descriptions of the Impacts

Parameter description	Range of values	Value pre-tuning	Value post-tuning	Expected impact of tuning
Threshold of relative humidity for cloud formation	0.600–0.900	0.700	0.605	More cloud forms under the same humidity (Irvine et al., 2013)
Lateral entrainment coefficient	0.600–9.000	3.000	2.789	This parameter controls the mixing of deep convective plumes with their surroundings. Therefore, more air convecting clouds can be drawn in from surrounding grid boxes (Irvine et al., 2013; Ross, 2023)
Cloud drop number (land) (drop/cm^3)	–	125	50	Precipitation rate increases, cloud lifetime becomes shorter and cloud cover reduces (Kiehl & Shields, 2013)
Cloud drop number (sea) (drop/cm^3)	–	70	50	–
Cloud drop radii (land) (μm)	–	13.500	17.000	–
Cloud drop radii (sea) (μm)	–	17.000	17.000	–
Threshold of liquid water for the formation of precipitation (over sea) (kg m^{-3})	2.000e^{-5} - 5.000e^{-4}	5.000e^{-5}	3.532e^{-5}	Conversion of cloud water droplets to rain increases and cloud lifespan decreases (Irvine et al., 2013; Ross, 2023; Rougier et al., 2009)
Threshold of liquid water for the formation of precipitation (over land) (kg m^{-3})	1.000e^{-4} - 2.000e^{-3}	2.000e^{-4}	1.606e^{-4}	–
Cloud droplet to rain conversion rate (s^{-1})	5.000e^{-5} - 4.000e^{-4}	1.000e^{-4}	2.690e^{-4}	–
Ice-fall speed (m/s)	0.500–2.000	1.000	1.339	Ice particle size increases, which is associated with decreases in cirrus cloud coverage, longwave cloud forcing and upper troposphere water vapor (Mitchell et al., 2011; Sanderson et al., 2008)
Minimum albedo of sea ice	0.470–0.650	0.500	0.610	Albedo driven feedbacks increase but are less important in warmer climates (Ross, 2023)
Background coefficient of vertical mixing of tracers at the surface	–	1.000e^{-5}	1.419e^{-5}	Stronger oceanic overturning and deep water formation increases (Ross, 2023)
Vertical diffusion rate of increase with depth (m s^{-1})	–	2.800e^{-8}	5.638e^{-8}	–
Solar constant (W/m^2)	–	1,365	1,361	Change made to be consistent with CMIP6 protocols

The objective approach involves generating a PPE - an ensemble of models with perturbed parameters within a plausible range, and then comparing the model outputs to identify the best fit to the observations (Irvine et al., 2013; J. M. Murphy et al., 2004). Parameters in Table 1 except for cloud drop numbers and cloud drop radii are objective tuning. Here, five atmospheric, one sea ice parameters and two oceanic parameters were perturbed by Irvine et al. (2013) which followed the elicitation in J. M. Murphy et al. (2004) except for the oceanic parameters which followed Collins et al. (2007) and Brierley et al. (2010): the threshold of relative humidity for cloud formation, the lateral entrainment coefficient, the threshold of liquid water for the formation of precipitation, the cloud droplet to rain conversion rate, the ice-fall speed, the minimum albedo of sea ice, the vertical diffusion rate of increase with depth and background coefficient of vertical mixing of tracers at the surface. Irvine et al. (2013) generated 200 versions of the HadCM3 with varied parameter combinations that sampled the parametric uncertainty using a maximum Latin hypercube sampling technique following Gregoire et al. (2011). Versions of HadCM3 which produced preindustrial temperatures outside the observed global mean (13.6 ± 2°C) were excluded. These models were also used in a quadrupled CO_2 simulation, and were compared to the Eocene proxy data qualitatively, considering polar temperature response to the increased CO_2 concentration (Ross, 2023). The parameter set except for the oceanic diffusion used in this study is the same as in Ross (2023), which quantitatively best fit modern observational data and qualitatively produce a higher polar amplification in response to a higher CO_2. In the study of Ross (2023) who used HadCM3BL-M2.1N - a lower resolution of HadCM3, three more parameters of oceanic vertical diffusion were tuned to make the ocean circulation closer to that of the original HadCM3.

10.1029/2024PA004976

The subjective approach targets a particular part of the system and aims to improve subgrid-scale physical processes. In this paper, cloud parameters—cloud drop number and cloud drop radii are modified following Kiehl and Shields (2013), with the aim of improving simulated cloud properties in past warm climate simulations as cloud can lead to significant changes in radiation. Since there are no observed cloud microphysical properties for warm periods in the geological past, Kiehl and Shields (2013) used observations of modern remote pristine regions from Ramanathan et al. (2001) to modify the cloud-relevant parameters. The values and impact of tuning on cloud drop number and cloud drop radii are as shown in Table 1.

The process-improvement tuning aims to improve representation of physical processes. There are four process-improvement tunings that are implemented in the HadCM3t of this study: (a) and (b). Remove grid-point noise by applying a smoothing in the atmospheric pressure field and the oceanic barotropic stream function field; (c). Adding bottom friction to the sediment water interface to avoid extreme values of the ocean velocities; (d). Applying a correction to the parameterization of gravity wave propagation (Ross, 2023).

Moreover, we also modified the solar constant to 1,361 W/m^2 to better fits the CMIP6 protocol. By implementing all these changes, we aim to tune the model to better represent mPWP reconstructed SSTs, especially at high latitudes, without changing its performance in simulating modern climate.

2.3. Energy Budget Analysis

In this study, two approaches of energy balance analysis are adopted: The one-dimensional energy balance model (EBM) and the APRP.

The EBM is a simple model that provides insights into the Earth's energy budget along the meridional dimension. Details and full descriptions can be found in Heinemann et al. (2009), Lunt et al. (2012) and Hill et al. (2014); these studies carried out the analysis for the Paleocene, Eocene and Pliocene, respectively. This method is used to quantify different contributors to the temperature anomaly between two simulations, and is commonly used to diagnose paleoclimate simulations (e.g., Chandan & Peltier, 2018; Hill et al., 2014; Lunt et al., 2021; Lohmann et al., 2022). Hill et al. (2014) carried out energy balance analysis for the PlioMIP1 simulations. EBM analysis includes both shortwave and longwave radiation, and shows the effects with temperature change. In this study, the components that contribute to the surface temperature change are decomposed into planetary albedo, emissivity, and heat transport by EBM. Emissivity is further decomposed into contributions induced by cloud changes and those associated with greenhouse effect and the lapse-rate effect. In EBM, in terms of the changes in shortwave radiation, the role of clouds is considered simply as a mask to reflect solar radiation, while the cloud does not just reflect the shortwave radiation but also affects the radiation through the TOA by absorbing and scattering shortwave radiation. Besides clouds, noncloud components in the atmosphere (such as CO_2) which absorb and scatter radiation are also important. This is particularly necessary in this study because one of the main differences between HadCM3t and HadCM3u are different cloud physical parameters, which can be seen in the comparison of cloud contributions between the mPWP and PI experiments.

Therefore, to further investigate contributions from the cloud and noncloud to the shortwave radiation, the APRP method is adopted in this study to analyze the radiative effect (RE) changes as described in Taylor et al. (2007). In a simulated Earth system, the model can provide monthly radiative flux data of outgoing and incoming flux of TOA and surface, as well as cloud cover and temperature. The APRP method is a simplified radiative transfer model that describes radiative flux changes in terms of atmospheric absorption, atmospheric scattering, and albedo. This method estimates the feedback parameter associated with shortwave feedbacks in climate models. Compared with the full PRP procedure introduced by Wetherald and Manabe (1988), the APRP method requires only a modest amount of monthly mean data and much less computational power, with satisfactory accuracy and much higher efficiency (Zelinka et al., 2023), and has been broadly used in paleoclimate simulation studies (e.g., Brady et al., 2013; Feng et al., 2017; Zhu et al., 2019). Although EBM and APRP provide results in terms of temperature and radiative effect (RE) changes separately, the RE components from APRP are converted into corresponding temperature changes by applying the results to the EBM.

2.4. Spin-Up of Simulations

Four simulations were carried out: preindustrial and mPWP using HadCM3u (abbreviated as PI_u and $mPWP_u$, respectively), and preindustrial and mPWP using HadCM3t (abbreviated as PI_t and $mPWP_t$, respectively). All four simulations were run for 2,000 years. By checking the top-of-atmosphere (TOA) radiation imbalance and global mean oceanic temperature trends at various depths (Figure S2 and S3 in Supporting Information S1), we consider all runs to have reached a sufficient level of equilibration.

Moreover, the full equilibrium global surface temperature can be deduced from Figure S4 in Supporting Information S1, which regresses net TOA radiation imbalance against surface air temperature change (the graphical illustration of this regression is referred to as a Gregory plot; Gregory et al., 2001). Compared to the first few hundred years, the average of the last one hundred years show a TOA radiation imbalance of less than 0.1 W/m^2 and a higher land surface temperature. At full equilibrium, the global surface temperatures for $mPWP_t$ and $mPWP_u$ are expected to become higher than those for PI_t and PI_u by 3.3°C and 3.1°C respectively, as shown in Figure S4 in Supporting Information S1. The mPWP and PI using HadCM3t show lower global mean surface temperatures than using HadCM3u, by 0.2°C and 0.4°C respectively. For the following sections, the average of the final 100 years for each experiment was analyzed.

4xCO_2 simulations are also carried out to calculate the effective climate sensitivity (ECS) for both models, following the methods from Gregory et al. (2004). The ECS in the HadCM3t is 2.99°C which is lower than the 3.48°C ECS value in HadCM3u (Figure S5 in Supporting Information S1).

3. Results

In this section, we first compare the modeled PI climate from HadCM3t and HadCM3u with observed preindustrial climate (Section 3.1). Then, in Section 3.2 we investigate the surface temperature anomaly differences between the mPWP relative to PI as simulated by HadCM3t and HadCM3u, and compare the model results with proxy reconstructions. Section 3.3 describes the differences observed for large-scale climatic features other than surface temperature in the modeled mPWP from HadCM3t relative to the associated PI controls, and in comparison with the results from HadCM3u. Sections 3.4 and 3.5 explain the different responses from HadCM3t and HadCM3u by using the EBM and APRP approaches.

3.1. Preindustrial Model-Observation Comparison

Model performance in terms of simulating preindustrial climate is assessed by comparison with reanalysis data (available at https://psl.noaa.gov/data/gridded/index.html) for eight different variables (SST, surface air temperature, precipitation, cloud coverage, surface specific humidity, ice concentration, TOA upwelling shortwave and TOA upwelling longwave) from the NOAA Extended Reconstructed SST V5 (ERSST v5) (Huang et al., 2017), the NOAA-CIRES-DOE Twentieth Century Reanalysis (20CRv3) (Slivinski et al., 2019) and the Measurements from the Clouds and the Earth's Radiant Energy System (CERES) observed data (available at https://ceres.larc.nasa.gov/data/). The reanalysis climate data from 1850 to 1900 (1854–1900 for SST and 2005–2015 for RSUT and RLUT due to data availability) is adopted to compare with the simulated PI climate. Both HadCM3t and HadCM3u simulate slightly warmer global mean SST and cooler global mean surface air temperature than the reanalysis data (Figures 1a and 1c and 1d). Both models also simulate a relative cooler Northern Pacific Ocean and North Atlantic Ocean, warmer Southern Ocean and cooler Polar Regions. In terms of precipitation, cloud cover, surface specific humidity (HUSS), ice concentration and RLUT (Figure 1), HadCM3t and HadCM3u show similar discrepancy with the reanalysis data in terms of the spatial pattern. Both models simulate more precipitation over the Maritime Continent, South Africa and northeastern South America, but drier climate over the tropical Pacific and North Atlantic Oceans. Regarding cloud cover, the models both simulate less cloud than the reanalysis by a global average of −11.14% (HadCM3t) and −11.69% (HadCM3u), with the most marked difference over tropical oceans. In terms of HUSS, HadCM3u simulates a more humid climate over the tropical oceans, whereas HadCM3t is closer to the reanalysis HUSS over the Maritime Continent and the eastern Pacific Ocean than HadCM3u. Both HadCM3t and HadCM3u underestimate ice concentration over high latitudes, especially around Antarctic. Regarding RSUT, the models simulate less RSUT over New Guinea and coast near Peru, and more RSUT over low to mid-latitude Ocean regions relative to modern observation. Both models overestimate RLUT over tropical western tropical Pacific Ocean, India and tropical America. Overall, compared to the reanalysis data, both models simulate higher SST, cooler surface air temperature, less precipitation, less cloud cover and less ice concentration.

10.1029/2024PA004976

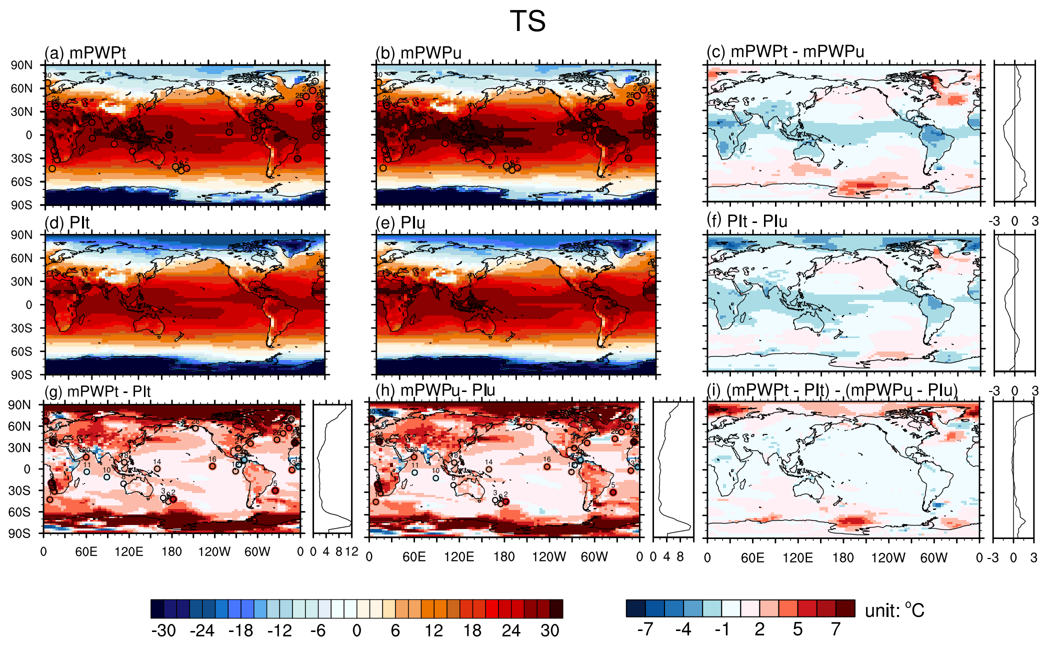

Figure 2. The annual mean surface temperature (TS) of simulations and their differences. (a) mPWP_t; (b) mPWP_u; (d) PI_t; (e) PI_u; (c) mPWP_t—mPWP_u; (f) PI_t—PI_u; (g) mPWP_t—PI_t; (h) mPWP_u—PI_u and (i) (mPWP_t—PI_t)—(mPWP_u—PI_u). The plots on the right side of the subfigures denote the zonal means. In panels (a, b), the circles represent the reconstructed SSTs of mPWP by colors (McClymont et al., 2020), and the number of each site is indicated on the top of each circle. In panels (g, h), the circles represent the reconstructed SSTAs. The differences between the reconstructed SSTs and simulated SSTs of the mPWP are as shown in Figures 3a and 3b; the differences between the reconstructed SSTAs and simulated SSTAs are as shown in Figures 3c and 3d. A Taylor diagram of the comparison between simulated and reconstructed sea surface temperatures of the mPWP in panels (a, b) is as shown in Figure S7 in Supporting Information S1.

3.2. Surface Temperature Anomaly—Comparison Between Models and mPWP Proxy Reconstruction

The simulated surface temperature (TS), their differences, and proxy SST reconstruction from McClymont et al. (2020) are as shown in Figure 2. Both mPWP_t and mPWP_u produce a warmer TS than PI_t and PI_u by 3.2°C and 2.9°C, respectively, especially over the high latitudes (Figures 2g and 2h). HadCM3t produces a zonal averaged warming peak over the North Pole by around 10°C and around Antarctica by over 12°C. The temperature anomaly from HadCM3t shows a larger polar amplification in the mPWP compared with HadCM3u. The polar amplification factors (warming polewards of 60°N and 60°S divided by the global mean warming) of HadCM3t is 2.2 (Table 2), which is higher than 2.0 from HadCM3u. The spatial pattern of this warming difference between HadCM3t and HadCM3u is concentrated in the Arctic, the North Atlantic, and the Southern Oceans (Figure 2i).

The model performance in simulating the mPWP SSTA and SST are evaluated by comparisons between the simulation and the multi-proxy reconstructed SSTA and SST (McClymont et al., 2020), as shown in Figure 3. The global averaged discrepancies between the reconstructed mPWP SSTA and the simulated SSTA from HadCM3t and HadCM3u, quantified using Monte Carlo simulations following the method described in Kageyama et al. (2021), are 1.98°C and 2.38°C, respectively, suggesting an improved model performance in reproducing SSTA after tuning (Figure 3e). The improvement is limited in the low latitudes. In the Polar Regions with available proxy data, HadCM3t still underestimates the warming but shows reduced discrepancies (Figures 3c and 3d). As shown in Figure 3e, HadCM3t produces a smaller discrepancy than HadCM3u over the mid-latitudes and Polar Regions, suggesting that a better representation of the mPWP SSTA in these regions accounts for the smaller global discrepancy in HadCM3t than HadCM3u. The simulated mPWP SST in HadCM3t aligns better with the reconstructed SST than in HadCM3u, as shown by the Taylor Diagram in Figure S7 in Supporting Information S1. The root mean squared error (RMSE) between the simulated SST in HadCM3t and the reconstructed SST is 2.17, which is lower than the RMSE of 2.84 in HadCM3u. Furthermore, applying HadCM3t for the mPWP while retaining HadCM3u for the PI reduces the global mean discrepancy with the reconstructed

Table 2
The Regional Mean of Temperature Changes From Different Components Estimated by the EBM and the Approximate Partial Radiative Perturbation Methods From Figure 9

	Temp change (GCM)	Temp change (EBM)	Emissivity			Heat transport	Surface albedo (shortwave)	Noncloud (shortwave)	Cloud (shortwave)			
			Sum	Cloud (longwave)	GHG&LR				Sum	Fraction	Scattering	Absorption
HadCM3t global	3.2	3.1	**1.8**	−0.1	**1.8**	0.0	0.9 (2.9)	0.3 (0.9)	0.1 (0.5)	0.5 (1.5)	−0.3 (−0.8)	−0.1 (−0.2)
Polar regions	7.0 [2.2]	7.2	**4.4**	0.8	3.6	−1.0	4.0 (12.1)	0.5 (1.6)	−0.3 (−1.0)	0.2 (0.5)	−0.4 (−1.3)	−0.1 (−0.2)
>60N	6.0 [1.9]	6.2	**3.8**	0.5	3.3	−1.3	3.3 (10.4)	0.5 (1.6)	0.3 (0.8)	0.5 (1.4)	−0.1 (−0.2)	−0.2 (−0.5)
<60S	8.0 [2.5]	8.3	**5.0**	1.0	3.9	−0.7	4.7 (13.9)	0.5 (1.5)	−0.9 (−2.7)	−0.1 (−0.3)	−0.8 (−2.4)	0.0 (0.1)
Tropical	2.1	1.8	1.3	−0.2	**1.5**	0.1	0.4 (1.4)	0.2 (0.7)	−0.1 (−0.4)	0.2 (0.8)	−0.3 (−1.1)	0.0 (0.0)
HadCM3u global	2.9	2.8	**1.7**	0.0	**1.7**	0.0	0.8 (2.6)	0.3 (0.9)	0.0 (0.0)	0.3 (1.1)	−0.3 (−0.9)	−0.1 (−0.2)
Polar regions	5.7 [2.0]	6.0	**3.8**	0.7	3.0	−0.9	3.3 (9.8)	0.5 (1.5)	−0.5 (−1.3)	0.2 (0.6)	−0.6 (−1.6)	−0.1 (−0.2)
>60N	4.8 [1.7]	5.0	**3.1**	0.4	2.6	−1.2	2.5 (7.7)	0.6 (1.7)	0.3 (0.9)	0.7 (2.1)	−0.2 (−0.6)	−0.2 (−0.6)
<60S	6.6 [2.3]	6.9	**4.4**	1.0	3.4	−0.5	4.1 (11.9)	0.5 (1.3)	−1.2 (−3.5)	−0.3 (−1.0)	−0.9 (−2.7)	0.1 (0.2)
Tropical	2.1	1.9	**1.6**	0.0	**1.6**	−0.1	0.4 (1.4)	0.2 (0.8)	−0.2 (−0.8)	0.1 (0.3)	−0.3 (−0.9)	−0.0 (−0.1)
Difference global	0.3	0.3	**0.1**	−0.1	**0.1**	0.0	**0.1** (0.3)	0.0 (0.0)	**0.1** (0.5)	0.1 (0.4)	0.0 (0.0)	0.0 (0.0)
Polar regions	1.3	1.3	0.6	0.1	0.6	−0.1	**0.7** (2.3)	0.0 (0.1)	0.1 (0.3)	0.0 (0.0)	0.1 (0.3)	0.0 (0.0)
>60N	1.2	1.2	**0.8**	0.2	0.7	0.0	**0.8** (2.6)	−0.0 (−0.1)	−0.1 (−0.2)	−0.2 (−0.7)	0.1 (0.4)	0.0 (0.1)
<60S	1.3	1.4	**0.6**	0.1	0.5	−0.2	**0.6** (2.0)	0.1 (0.3)	0.3 (0.8)	0.2 (0.6)	0.1 (0.3)	−0.0 (−0.1)
Tropical	−0.1	−0.1	**−0.3**	−0.2	−0.1	0.2	−0.0 (−0.1)	0.0 (0.0)	0.1 (0.3)	0.1 (0.5)	−0.1 (−0.2)	0.0 (0.1)

Note. Polar Regions here are regions 60°N and 60°S polewards. The polar amplification factor (the ratio of warming poleward of 60°N and 60°S to the global mean warming) are shown in square brackets. The unit is °C. The changes in shortwave radiative effect (RE) from APRP components are shown in round brackets, which have the unit of W m^{-2}. Here GHG&LR denote greenhouse effect and lapse-rate effect. The dominant contributor in each category is indicated in bold.

SSTA (Figure S8 in Supporting Information S1), implying that the improved alignment of the mPWP SSTA from HadCM3t with the reconstruction is primarily due to the better simulation of the mPWP.

3.3. Documentation of Non-Temperature Climatic Features

In this subsection, other climatic features of the mPWP and PI produced by HadCM3t and HadCM3u are described in terms of atmospheric variables and oceanic states. First, the mPWP climatology anomaly relative to the PI produced by HadCM3t will be described in terms of fresh water flux (precipitation minus evaporation; P-E) (Figure 4), total cloud amount (Figure 5), atmospheric vapor (Figure 6) and ice fraction (Figure 7) in Section 3.3.1, and oceanic meridional overturning circulation (Figure 8) in Section 3.3.2. After the description of each climatic feature, the differences in climatology anomalies of the mPWP relative to the PI from the two models are discussed. The spatial pattern of climatology fields of the mPWP and the PI from both models and their differences are all shown. The differences between HadCM3t and HadCM3u in the same experiments are also

10.1029/2024PA004976

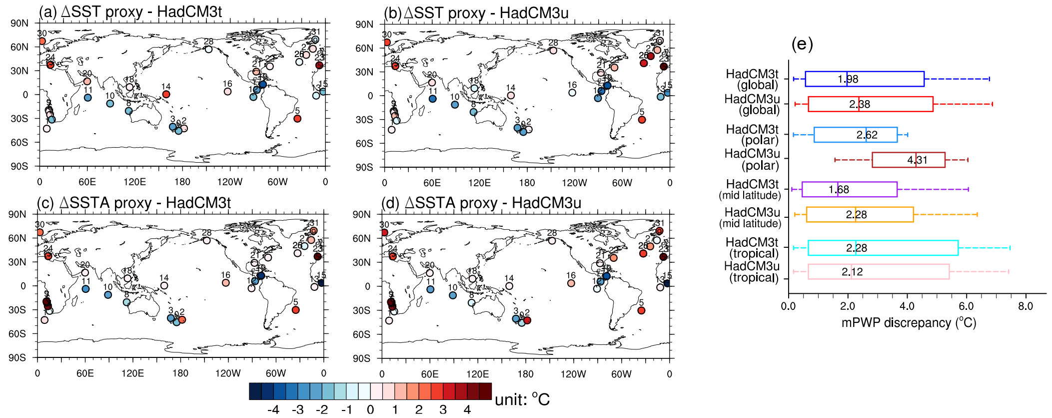

Figure 3. (a, b) The difference between the reconstructed mPWP sea surface temperatures (SST) from McClymont et al. (2020) (Figures 2a and 2b) and the mPWP SST from models. (c, d) The difference between the reconstructed mPWP SSTA relative to PI from McClymont et al. (2020) (Figures 2g and 2h) and the mPWP SSTA from models. (e) Box plots showing discrepancies between model simulations and proxy-based SSTA for global and regional scales. Vertical lines inside the boxes are the median values of the possibility distribution function of the discrepancies derived via Monte Carlo simulations considering the uncertainties of the reconstructed SSTAs. Lower and upper box boundaries indicate the interval where the model and proxy discrepancies are likely to be (probability range from 66% to 100%). Lower and upper error lines indicate the interval where the model and proxy discrepancies are most likely to be (probability range from 90% to 100%). The unit is °C. Details of this metric can be found in Ren et al. (2023). Polar Regions indicate regions polewards of 60°N and 60°S. The mid-latitudes here refer to the regions between 23.5° and 60° in both the Northern and Southern Hemispheres.

included here to discuss the effect of tuned parameters on both the PI and the mPWP, but will be explored further in Section 4.2.

3.3.1. Atmospheric Features

A higher global surface temperature will in general result in an increase in global precipitation (Andrews et al., 2010; Frieler et al., 2011). Figure 4 shows the simulated P-E of the mPWP and the PI from both models (the changes in precipitation are shown in Figure S9 in Supporting Information S1). HadCM3t and HadCM3u produce similar P-E anomalies of the mPWP relative to the PI, with the most significant changes over the low latitudes

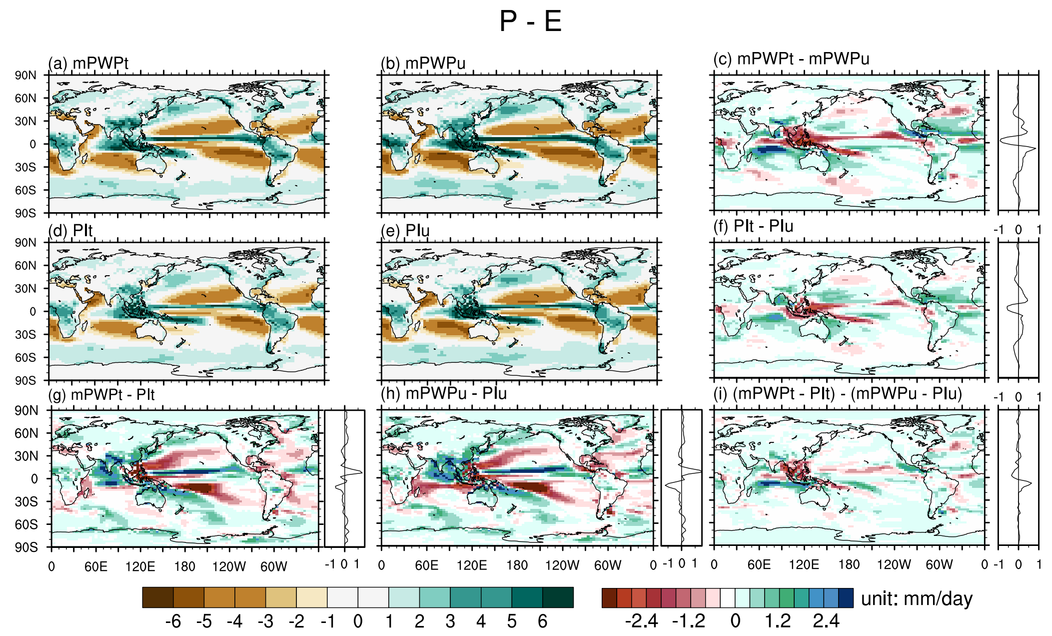

Figure 4. The same as Figure 2 but for fresh water flux precipitation minus evaporation (P–E).

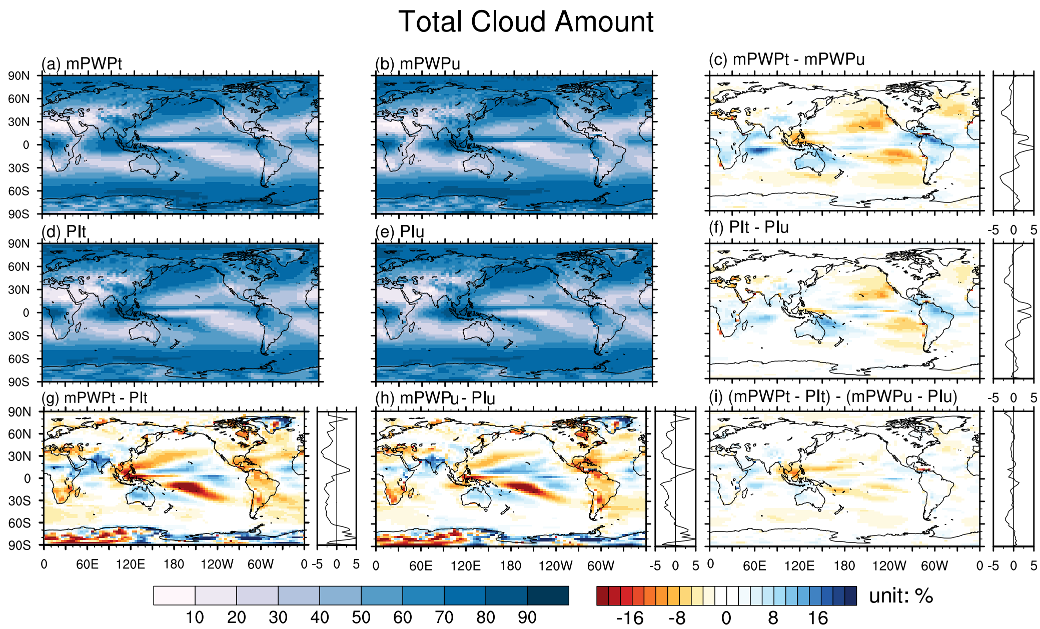

Figure 5. The same as Figure 2 but for total cloud amount.

(Figures 4g and 4h). The zonal average shows that the P-E increases significantly over the northern tropics and decreases over the southern tropics (Figure 4g). Although HadCM3u produces a similar pattern over the tropics, the P-E anomalies are more extreme than those from HadCM3t (Figure 4h). The spatial pattern is also slightly different with HadCM3t simulating less extreme P-E anomaly values over the tropical Pacific Ocean than HadCM3u. Generally, the areas with increased or decreased P-E anomaly are similar between HadCM3t and HadCM3u.

Precipitation is linked to cloud cover. Clouds are also very important in regulating the Earth's energy system via their high albedo and their greenhouse warming effect. Figure 5 illustrates the spatial pattern of cloud cover and cloud cover anomaly from HadCM3t and HadCM3u. Compared to the PI, cloud cover increases over the northern

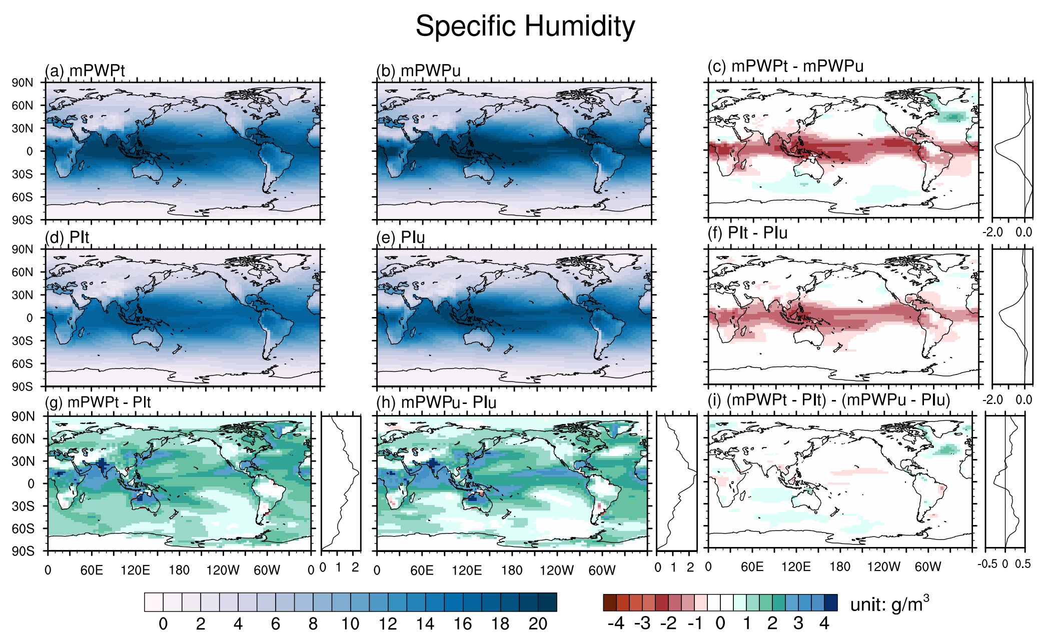

Figure 6. The same as Figure 2 but for surface specific humidity (HUSS).

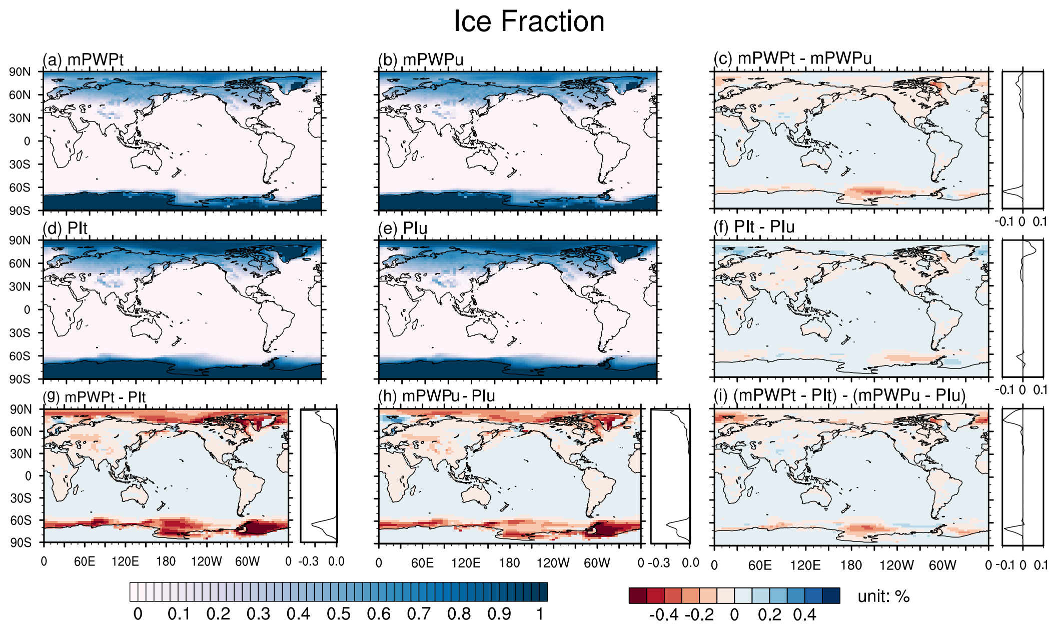

Figure 7. The same as Figure 2 but for total ice fraction (sea ice, land ice and snow cover).

tropics, northern Greenland, and around Antarctica, but decreases over the rest of the globe in the mPWP (Figure 5g). Over the low latitudes, the P-E anomaly has a similar distribution to the cloud cover anomaly, as well as to atmospheric ascent at 850 hPa (Figure S10 in Supporting Information S1), which implies the P-E anomaly changes with the cloud cover anomaly, or that they are both influenced by the atmospheric ascent over the low

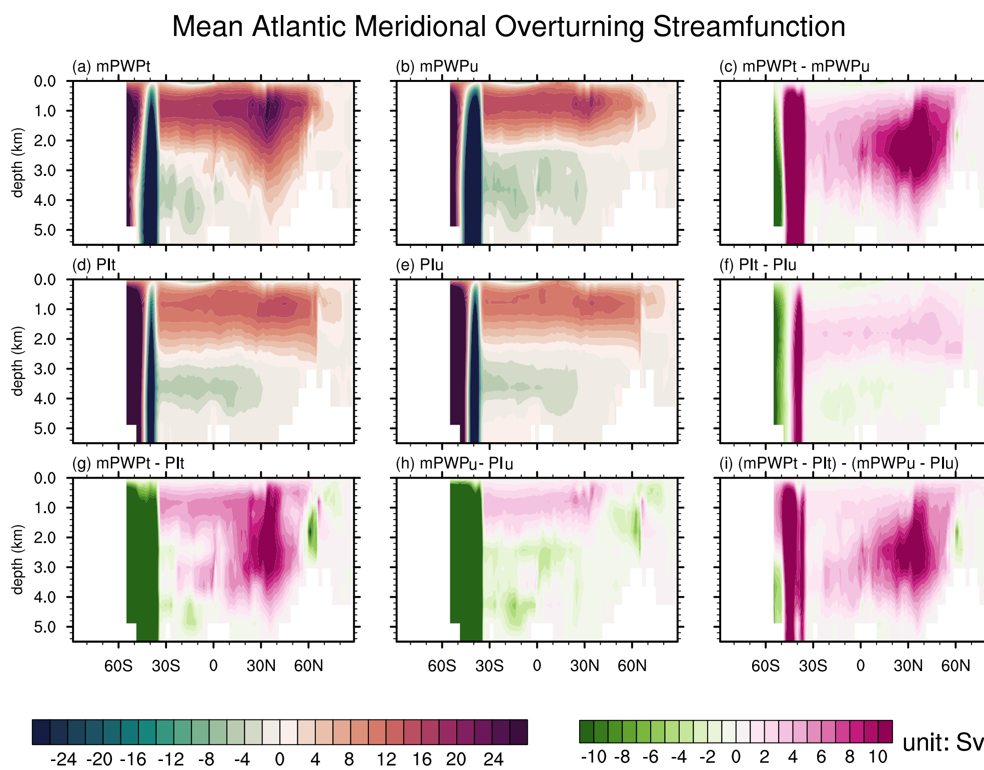

Figure 8. The Atlantic Meridional Overturning Circulation stream function in sverdrups (Sv). Positive and negative values indicate clockwise and anticlockwise overturning, respectively. The white colors indicate the land.

latitudes. The cloud cover is also highly influenced by atmospheric humidity and temperature. Over the land surface, the cloud cover anomaly changes are consistent with the atmospheric relative humidity (Figure S11 in Supporting Information S1). HadCM3t generates a similar cloud cover anomaly to HadCM3u. Compared with HadCM3u, the cloud cover anomaly from HadCM3t increases less over the northern tropics and the northern high latitudes, and decreases more over the southern mid-latitudes, but decreases slightly less over the southern pole, southern tropics, and areas around 20°N (Figure 5i).

In addition to the cloud and CO_2, atmospheric water vapor will contribute to temperature change via the greenhouse effect, and through absorption of solar radiation. The surface specific humidity (HUSS) of the mPWP and the PI from HadCM3t and HadCM3u and their differences are as shown in Figure 6. HUSS is dominated by TS (Figure 2) and evaporation (Figure S12 in Supporting Information S1) due to the Clausius-Clapeyron relationship. As the mPWP is warmer than the PI, the HUSS increases over almost the entire globe, with a peak over the northern tropics and then relatively less but still substantial high HUSS over the high latitudes. Relative to the HUSS changes from HadCM3u, HadCM3t has a relatively smaller increase in HUSS over the tropics; whereas over the high latitudes, HadCM3t has a higher increased HUSS, which is consistent with the changes in TS and evaporation (Figures 2i and 6i and Figure S12i in Supporting Information S1).

Regarding the Earth's energy balance, the change in sea ice and snow cover is very important for shortwave radiation due to its high albedo and the significant difference from the mPWP to PI. Changes in sea ice are very sensitive to temperature change. As the high latitudes warm significantly in the mPWP compared to the PI, there is substantial sea ice loss over the high latitudes as well as the prescribed reduction in land ice and snow coverage (Figures 7g and 7h). Due to higher TS warming, there is more sea ice loss over the high latitudes in HadCM3t simulated mPWP compared to HadCM3u simulated mPWP (Figure 7i). Compared to the changes in the cloud cover, the regions of Greenland and Southern Polar region with sea ice fraction loss are also regions with substantial increase in cloud. Although HadCM3t and HadCM3u are initialized with a fixed terrestrial ice sheet which already includes topographic differences, the substantial sea ice loss can still emphasize the topographic changes and therefore causes the cloud cover to change. Additional future sensitivity studies could explore the relative impact of the sea ice albedo tuning versus other parameters (Howell et al., 2014).

3.3.2. Oceanic Features

The tuned parameters of the model influence the atmosphere, the sea ice, and the ocean. In terms of the modification to the model, the simulated ocean situation is directly influenced by two tuned parameters—the vertical mixing of momentum coefficient (J. Murphy et al., 2009) and vertical diffusion rate of increase with depth (Irvine et al., 2013), which are expected to instigate stronger oceanic overturning after tuning (Table 1). The Atlantic Meridional Overturning Circulation (AMOC) of the mPWP and PI from HadCM3t and HadCM3u are as shown in Figure 8. The meridional overturning of the global, Pacific Ocean and Indian Ocean are shown in Figures S13–S15 in Supporting Information S1. The AMOC becomes stronger in the north in the $mPWP_t$ compared to PI_t which significantly intensified the global meridional overturning in the Northern Hemisphere (Figure S13 in Supporting Information S1). The AMOC differences between $mPWP_u$ and PI_u is much less significant. Moreover, model tuning changes AMOC in the mPWP but has much less influence on the PI (Figures 8c and 8f). The intensified AMOC from HadCM3t can also be inferred from the warmer ocean surface temperature over the high latitudes, especially the northern Atlantic, where it warms the most in the mPWP following tuning (Figure 2c), as the transport of warm water from the low latitudes strengthens. Regarding the Southern Hemisphere, meridional oceanic overturning changes the most at 60°S where directions of overturning at around 3,000 m depth change between the mPWP and the PI. Overall, a key feature of the mPWP oceanic anomaly after model tuning is the intensification of AMOC.

3.4. Earth System Energy Budget Analysis

To identify the reason for the higher mPWP polar TS anomaly in HadCM3t compared to HadCM3u, the Earth's energy imbalance between the mPWP and the PI is quantified by adopting the EBM and APRP approaches in terms of longwave radiation and shortwave radiation components. In this section, the zonal averaged and global averaged contributions from different components to the temperature changes between the $mPWP_t$ and PI_t from HadCM3t are first described. In terms of the shortwave components, there are the detailed APRP decomposition

10.1029/2024PA004976

of the shortwave radiative effect (RE) changes from surface albedo, cloud and noncloud components. Following this, the main focus is to compare the mPWP temperature anomalies simulated by HadCM3t and HadCM3u.

3.4.1. The mPWP Anomaly From HadCM3t

From the energy balance analysis for both HadCM3 models, it can be seen that the changes in the EBM components in the mPWP relative to the PI are very similar between HadCM3t and HadCM3u: the surface albedo and emissivity contribute the most to the mPWP global warming and polar region warming (Figure 9 and Table 2); other components have secondary influence in the mPWP warming anomaly. In HadCM3t, surface albedo and emissivity contribute 0.9°C and 1.8°C, respectively, to the global mean warming. The emissivity term is further decomposed into a small negative contribution from clouds variations (−0.1°C) and a dominant contribution from greenhouse gases and lapse-rate effects (GHG&LR) (1.8°C). In HadCM3u, surface albedo and emissivity contribute 0.8°C and 1.7°C, respectively, with the emissivity contribution primarily attributed to GHG&LR effects (1.7°C). The heat transport component has only regional impacts on the temperature change. The solar radiation component does not change mPWP temperature anoamly simulated by both models since the solar constant remains the same in the same model, therefore, it is not shown here.

Regionally, the emissivity-induced warming changes correspond with TS, which shows maxima warming anomaly near 80°S and in the Arctic. Emissivity and another major contributor, surface albedo, show similar changes over most regions but differentiate significantly around the tropics. Over the area around 10°N, changes in emissivity lead to significant temperature increase, while surface albedo leads to small changes. The emissivity-induced warming peak at around 10°N can be explained by the increase in cloud cover and the peak of surface specific humidity at around 10°N (Figures 5g and 6g), which leads to strengthened cloud-induced emissivity and GHG&LR-induced emissivity (dashed green lines in Figure 9). The cloud-related emissivity change shows a small contribution in the global mean, but contributes positively to polar warming (Figure 9 and Table 2). In the polar region, HadCM3t attributes 4.0°C of warming to surface albedo and 4.4°C to emissivity, including a 0.8°C contribution from longwave cloud effects. In comparison, HadCM3u attributes 3.3°C to surface albedo and 3.8°C to emissivity, with 0.7°C from longwave cloud effects. Although the cloud-induced emissivity change shows a small contribution to the global mean, but contributes positively to polar warming (Figure 9 and Table 2).

The contributions from shortwave associated components (surface albedo, noncloud and cloud) can be shown as RE changes with more details in Figure 10 (Figure S16 in Supporting Information S1 for HadCM3u). Regarding the surface albedo, the increased surface albedo-induced warming over the high latitudes can be explained by the mass loss of ice fraction. The surface albedo induced RE anomaly in both clear sky and overcast situations is most significant over regions (Figure 10Aa) where the majority of the surface is covered by ice in both the $mPWP_t$ and the PI_t (Figure 7). The surface albedo is largely influenced by the snow cover over the land and sea ice concentration over the ocean, regions that lose ice mass have much lower albedo and therefore reflect less radiation, so that albedo-induced RE under clearsky and overcast situations both increase significantly. The ice fraction does not decrease over all the high latitudes, for example, the ocean around Scandinavia where sea ice concentration increases, albedo-induced RE decreases. For regions fully covered by ice, like eastern Greenland and Antarctic in the $mPWP_t$ and the PI_t, the RE induced by the surface albedo doesn't change. Although the surface albedo-induced mPWP warming is relatively small compared to the high latitudes, changes in the surface albedo also cause RE to change over land in mid to low latitudes due to land surface type changes (Figure 10Aa). Here, changes in the surface albedo calculated from surface type without considering snow (Figure S17 in Supporting Information S1 using snow-free albedo calculations as described in Essery et al. (2001)) are consistent with the surface albedo induced RE change over the mid to low latitudes. The surface type change leads to a reduction in surface albedo over regions such as the northern tropical Sahara, Western Asia and the northern Australia, and therefore a significant increase in the RE due to surface albedo change, and vice versa over regions such as the south of northern Asia and North America. For example, the surface type adopted by each experiment (Figure S1 in Supporting Information S1) shows that the northern tropical Sahara and Western Asia changes from broadleaf tree, C4 grass and shrub to soil which has a lower albedo in the mPWP relative to the PI, and therefore a positive RE change.

The noncloud-induced shortwave RE increased by 0.9 W/m^2 from HadCM3t in the $mPWP_t$ compared to the PI_t, leading to 0.3°C warming (Figure 10Ad). Regions that are ice free in the $mPWP_t$ but covered by ice in the PI_t (e.

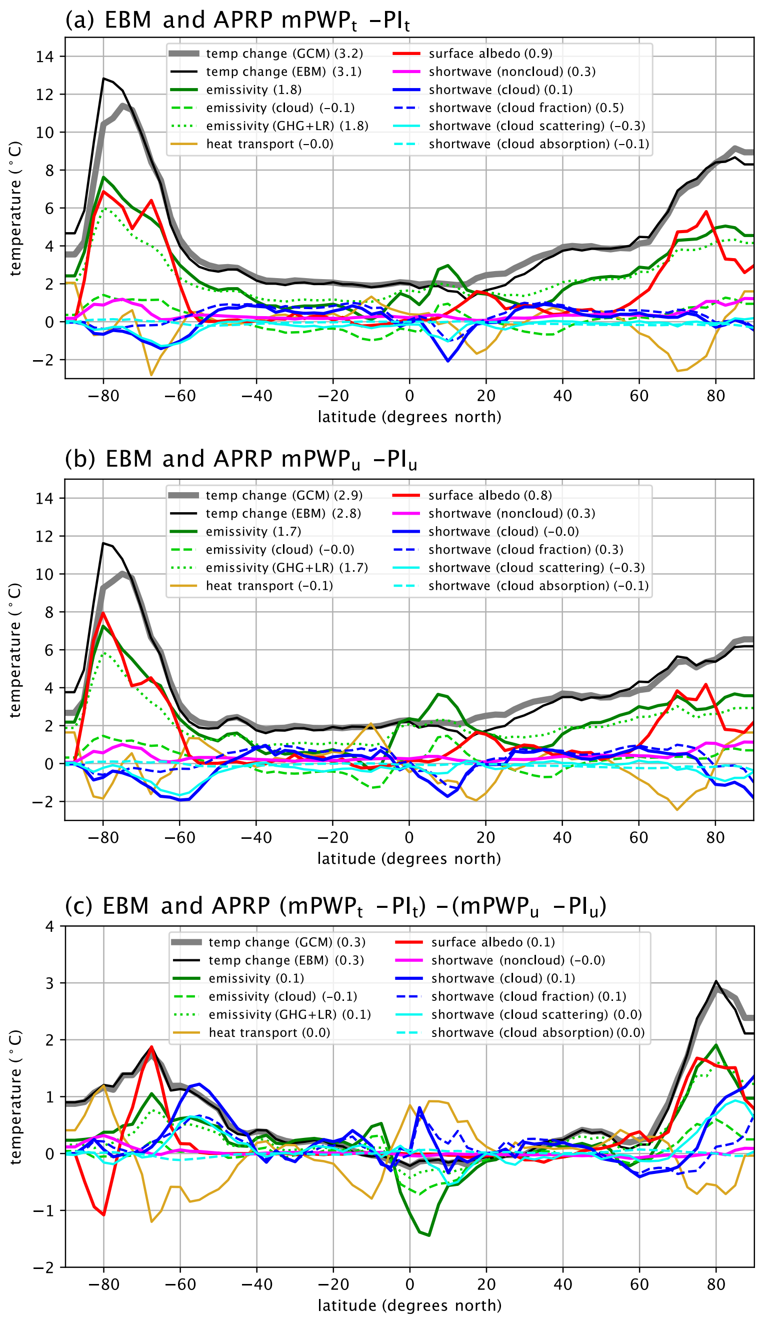

Figure 9. The results of the one-dimensional energy balance model (EBM) and the approximate partial radiative perturbation (APRP) analysis, as described in Section 2.4. (a) The EBM and APRP result of the energy imbalance between the $mPWP_t$ and PI_t, (b) the EBM result of the energy imbalance between the $mPWP_u$ and PI_u, and (c) the difference between HadCM3t and HadCM3u. These lines show the zonal mean of surface temperature changes (gray lines), temperature changes derived from the energy budget (black lines), and individual contributions from emissivity (green lines), decomposition of the emissivity component (greenhouse effect and lapse-rate effect (GHG&LR); green dash lines), meridional heat flux (orange lines), surface albedo (red lines), shortwave noncloud factor (magenta lines), shortwave cloud factor (navy blue lines) and decomposition of shortwave cloud factors (dash lines and cyan lines). Numbers after each component are the global mean value with the unit of °C.

g., the low-lying Wilkes and Aurora subglacial basins, West Antarctica, and western Greenland; Figure S18a in Supporting Information S1) are also regions where noncloud induced RE increase significantly. Here ice sheet changes between the mPWP and the PI lead to significant decreases in topography (by more than 1,500 m over

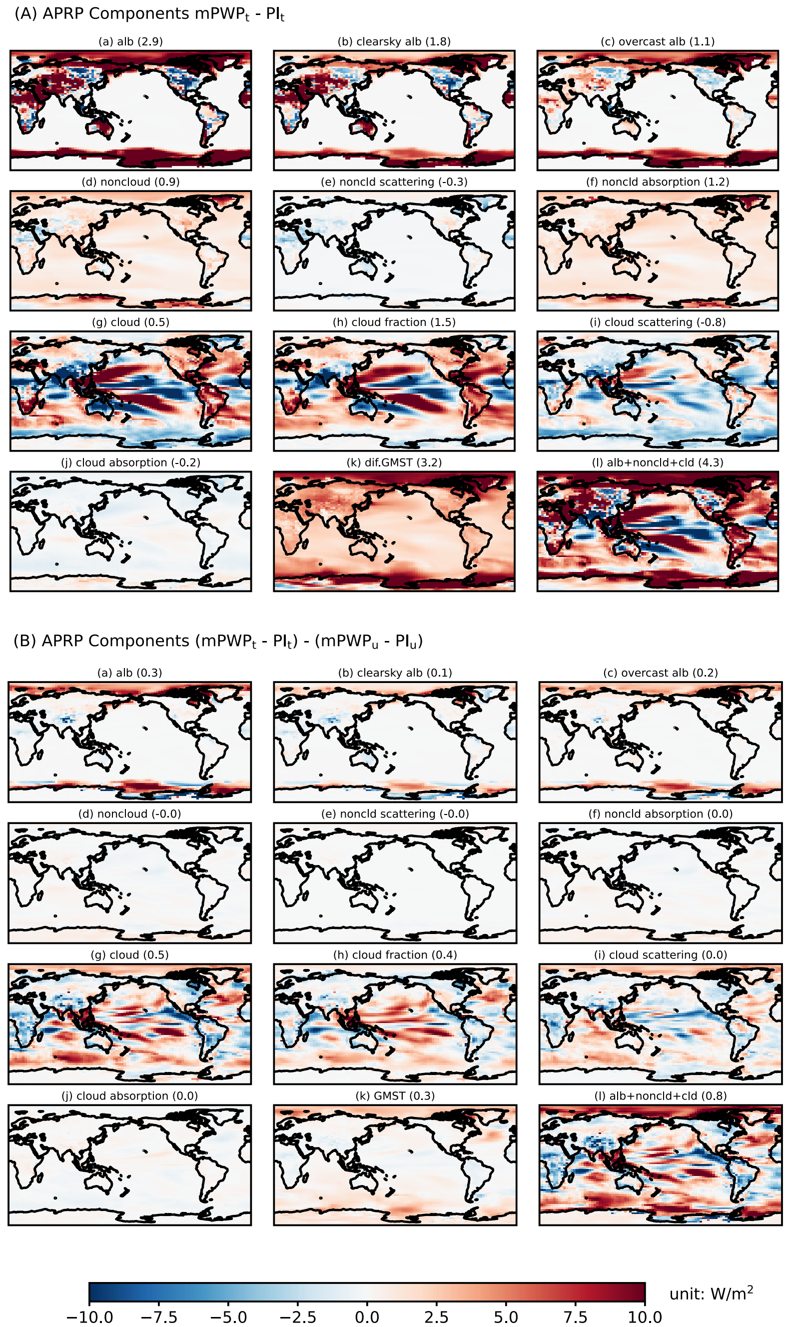

Figure 10. The contribution to the shortwave radiative responses from individual components as estimated by the approximate partial radiative perturbation method. (a) The mPWP anomaly from HadCM3t, and (b) the differences in mPWP anomaly between HadCM3t and HadCM3u. Here, (a) the contribution from surface albedo is the sum of contributions from (b) surface albedo under clearsky situation and (c) overcast situation. (d) The contribution from the noncloud factor is the sum of contributions from (e) clearsky scattering effect and (f) clearsky absorption. (g) The contribution from cloud factor is the sum of contributions from (h) cloud fraction changes, (i) cloud scattering effect and (j) cloud absorption. (k) Shows the global mean surface temperature (GMST) change directly from the model outputs with the unit of °C. (l) Shows the sum of RE change from the surface albedo, the noncloud and the cloud. All images except (k) have units of W/m^2. The numbers in brackets are the global mean for each individual component.

some regions), hence substantial increases in the thickness of the atmosphere and a positive RE change. For lands of mid to low latitudes, the noncloud-induced RE change is opposite to the surface albedo-induced RE, which can be explained by any increase in shortwave reflection increasing noncloud-induced RE, and vice versa. Moreover, in the APRP approach (Taylor et al., 2007), the increased CO_2 is also counted as a term that can lead to a positive RE.

The shortwave cloud contributes 0.1°C global average warming in the $mPWP_t$ relative to PI_t due to shortwave RE increases by 0.5 W/m^2. Further decomposition shows that the contribution from the cloud fraction effect (0.5°C warming; 1.5 W/m^2 RE) is counterbalanced by cloud scattering effect (−0.3°C temperature change; −0.8 W/m^2 RE) and cloud absorption effect (−0.1°C temperature change; −0.2 W/m^2 RE). Zonal average results (Figure 9a) show that the mid-latitudes warming, especially over the Southern Hemisphere mid-latitudes, is largely attributed to the cloud-induced RE anomaly. The distribution of cloud fraction-induced shortwave RE change corresponds inversely with the changes in the cloud amount (Figure 5g), but the impact is not proportional. For example, increased cloud fraction induces a reduction in RE over regions with increased cloud amount such as the Indian subcontinent and Sahara, and vice versa. For regions like Antarctica and Greenland where cloud amount changes substantially, the cloud fraction-induced RE does not change as much. This is because the total incoming shortwave radiation is much lower over the high latitudes than the low latitudes, therefore the cloud coverage change has a more significant impact on the low latitudes than the high latitudes. Moreover, the high albedo of ice sheets in Antarctica and Greenland reflect shortwave radiation even in the absence of clouds, resulting in minimal cloud impact on net radiation in these regions. The cloud scattering-induced shortwave RE also varies inversely with cloud coverage across most regions, but it exhibits different changes in regions, such as the subtropical Atlantic Ocean and northeastern Indian Ocean, where there is less cloud but stronger scattering effect which leads to a reduction in RE in both HadCM3t and HadCM3u. This can be explained by the changes in cloud characteristics involved in this study, which in this tuning exercise are cloud drop number and cloud drop radii. In terms of the zonal average, the cloud scattering-induced RE decreases significantly at around 65°S and 10°N due to the increased cloud amount, which results in a negative global mean of the cloud scattering-induced RE change. In comparison with the cloud fraction and scattering effect, the cloud absorption effect is small, and it makes insignificant differences in the APRP analysis.

3.4.2. Comparison Between HadCM3t and HadCM3u

The temperature anomalies and RE anomalies from different components of HadCM3t and HadCM3u are similar (Figures 9 and 10a, and Figure S19 in Supporting Information S1). On a global average perspective, the emissivity, surface albedo and shortwave cloud all contribute to the differences in temperature anomaly between HadCM3t and HadCM3u by +0.1°C, respectively (Figures 9c and Table 2); while shortwave noncloud factors and heat transport make neglectable contributions to the temperature anomaly change between models. Over the high latitudes, changes in emissivity, heat transport, surface albedo and cloud all make contributions to the warmer high latitudes mPWP anomaly from HadCM3t in relative to HadCM3u.

Emissivity-induced temperature anomaly increases in the northern and southern high latitudes, but decreases around the equator. These differences in emissivity-induced warming between HadCM3t and HadCM3u can be further attributed to the cloud-induced and GHG&LR-induced components (Figure 9), which are relevant to the differences in cloud anomalies and HUSS anomalies from HadCM3t and HadCM3u (Figure S20 in Supporting Information S1, Figures 5i and 6i). Over high latitudes where HUSS anomaly increases, the GHG&LR-induced warming increases coherently; in regions around the equator where HUSS anomaly decreases, the GHG&LR-induced warming decreases. In high latitudes, a higher temperature anomaly brings an increased HUSS anomaly, and therefore positive GHG&LR-induced warming; this forms a temperature–vapor–emissivity positive feedback. The heat transport changes contrarily with emissivity over the low latitudes and changes contrarily with albedo over the high latitudes.

In addition to the emissivity, there are differences in the contribution of surface albedo and cloud by influencing the shortwave RE between HadCM3t and HadCM3u. The changes in surface albedo contribute to a global mean temperature anomaly of 0.1°C and a 0.7°C increase in high latitudes, driven by surface albedo-induced RE increases of 0.3 and 2.3 W/m^2, respectively. As discussed above, it is the ice fraction loss that leads to the increased albedo-induced RE over high latitudes in HadCM3t. This linkage can also explain the difference in the albedo-induced RE anomaly between HadCM3t and HadCM3u, as there is less ice in HadCM3t simulated mPWP compared with HadCM3u simulated mPWP (Figure 7c), but there is more ice in HadCM3t simulated PI than HadCM3u simulated PI (Figure 7f). The same tuning processes lead to different ice fraction responses between the mPWP and the PI, which is the reason for the surface albedo-induced RE change, and can be seen in the APRP results in the same experiment from different models (Figure S21 and S22 in Supporting Information S1). In terms of temperature, HadCM3t produces warmer polar regions in the mPWP compared to HadCM3u (Figure 2c), leading to ice loss in the Arctic and around Antarctica (Figure 7c). Whereas in the PI, HadCM3t produces cooler Arctic temperatures and reduced warming around Antarctica (Figure 2f), with a corresponding ice response (Figure 7f). Hence, the temperature–ice–surface albedo positive feedback plays a crucial role in the amplified polar warming from HadCM3t than HadCM3u (Figure 2i).

The cloud component makes the largest shortwave RE contribution among the various components contributing to the difference between $mPWP_t$ and $mPWP_u$ anomalies, leading to a global average RE change of 0.5 W/m^2, which is equivalent to 0.1°C warming. In contrast, cloud-induced changes in emissivity contribute a cooling effect of −0.1°C to the difference in global mean temperature anomalies. Further decomposition of the shortwave cloud component shows that the cloud fraction makes the most significant difference, followed by cloud scattering, which contributes little to a global average, but largely influences the northern high latitude warming, along with the cloud fraction (Figures 9c and 10b). In contrast, the absorption factor has little influence on either the global average or spatial patterns. In terms of the global average, the larger cloud fraction-induced RE anomaly from HadCM3t is than HadCM3u can be explained by the corresponding decreased cloud amount anomaly around 50°S, 10°N (Figures 5i and 9c).

The energy budget analysis results from the same experiment but tuned and untuned HadCM3 reveal that the tuning process makes a strong difference in the cloud scattering effect, especially over regions with high cloud amount with the exception of the polar regions (Figures S21 and S22 in Supporting Information S1 and Figure 5). This is because the tuning process increasing cloud drop radius and decreasing cloud drop number, which causes a positive cloud scattering-induced RE anomaly. However, the drop radius and number of cloud are also influenced by other factors such as changes in humidity, atmospheric movement, temperature, etc. Overall, after model tuning, changes in the cloud lead to a substantial warming effect due to changes in shortwave RE. The combined effect of the tuning process and the changes in cloud cover itself leads to slightly different responses in cloud scattering-induced RE over some regions between the mPWP and the PI (Figure S21i and S22i in Supporting Information S1).

To summarize, the effect of emissivity on longwave radiation, along with the contributions of surface albedo and shortwave cloud component, each contributes to a +0.1°C difference in the mPWP TS anomaly between HadCM3t and HadCM3u. The warming resulted from the surface albedo component is because of 0.3 W/m^2 RE increase due to ice loss; the warming attributed to shortwave cloud component is due to 0.5 W/m^2 RE increase mainly from changes in cloud fraction.

4. Discussion

4.1. Comparison With PlioMIP2 Models

Using the same experimental design as other PlioMIP2 models allows us to compare tuned HadCM3 directly with PlioMIP2 models in simulating the preindustrial and the mPWP. HadCM3t has a similar performance in PI simulation to HadCM3u, yet outperforms HadCM3u and most PlioMIP2 models in simulating SSTAs of the mPWP (Figure 11a). The quantification of performance in simulating SSTAs of the mPWP is as described in Section 3.2 and caption of Figure 3, which is the median values of the possibility distribution function of the discrepancies derived via Monte Carlo simulations. In terms of the PI, tuned HadCM3 and untuned HadCM3 produce similar root-mean-square error (RMSE) compared with the ERSST v5 (Huang et al., 2017) SST climatology of 1854–1900, which are 1.40°C and 1.47°C, respectively (Figure 11a; Details are shown in Figures 1a and 1b).

The similarity between models can be deduced from the spatial correlation and the hierarchical clustering metrics based on the spatial features of SSTAs and precipitation from individual models, which also been used in Ren et al. (2023), the less the distance between models is, the more similar these models are. The performance of tuned HadCM3 and untuned HadCM3 are very similar in terms of reproducing global average PI SST and patterns of spatial anomalies. Figures 11b and 11c shows that among PlioMIP2 models and HadCM3t, the two closest model are HadCM3t and HadCM3u, that is, the most similar model for HadCM3u is HadCM3t regarding their simulated mPWP SSTAs and precipitation anomalies.

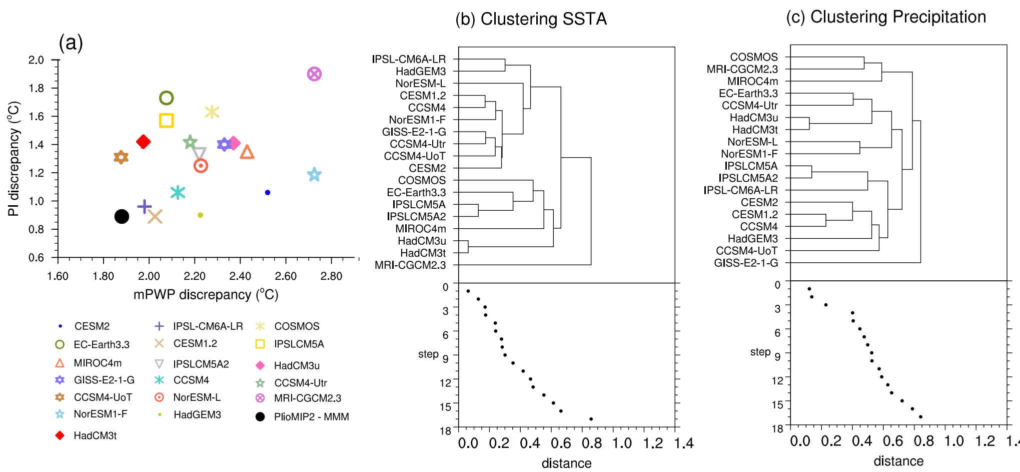

Figure 11. (a) The model-data discrepancies of the E280 and Eoi400 simulations from PlioMIP2 models and HadCM3t. The unit is °C. The quantification of the mPWP discrepancy is as described in Section 3.2. The PI discrepancy denotes the root-mean-square error (RMSE) between simulated PI and observation. (b, c) Dendrogram of the SSTA clustering analysis based on the global mean SSTAs and precipitation from 17 PlioMIP2 models (including HadCM3u) and HadCM3t. Below the dendrogram, the clustering step is shown as a function of distance between groups.

4.2. Synthesis of the Effect of Parameters on the Atmosphere

The atmospheric hydrological cycle is sensitive to model tuning and SST feedbacks. These factors, including humidity, cloud, and precipitation, also influence the Earth's energy balance. In the following text, we discuss the changes of atmospheric characteristics due to model tuning.

After tuning, specific humidity in the troposphere decreases significantly in almost all layers over all latitudes. The exceptions are a slight increase in near surface humidity over part of the mid-latitudes in the PI and over mid-latitudes and high latitudes in the mPWP (Figures S23 in Supporting Information S1). Zonal averaged results for evaporation, SST, and the near surface specific humidity change synchronously, implying that the changes in near surface humidity are dominated by SST and evaporation. Except for the near surface, the specific humidity generally decreases over all latitudes, with the largest decrease over the tropics. The large decrease over the tropics can be explained by the decreased water vapor supply due to decreased evaporation and weakened air ascending over the tropics (Figures S12 and S10 in Supporting Information S1). For regions of 35°N to 65°N and 40°S to 65°S, near surface humidity increases, which can be explained by the increased surface evaporation and the surface air ascending anomaly (Figures S10c, S10f and S12 in Supporting Information S1). However, the humidity in the upper troposphere over mid-latitudes still decreases, which may be a result of the weakened Hadley circulation and less tropical humidity that weaken the vapor transport into the upper troposphere (Figures S10 in Supporting Information S1 and Figure 6).

In terms of the stratosphere, specific humidity changes are insignificant following model tuning. Irvine et al. (2013) conducted experiments with different tuned parameters in HadCM3 and found that lower lateral entrainment coefficient values of less than 2.5 combined with higher CO_2 concentrations can cause a significant increase in high latitude stratospheric humidity. This change is also associated with higher climate sensitivity and higher temperature. Sanderson and Shell (2012) attributed higher climatic sensitivity with a large, positive longwave feedback to the upper atmospheric humidity increase. In our study, the lateral entrainment coefficient value was reduced from 3.000 to 2.789 but since this is still higher than 2.500 (Table 1) the influence of tuning this parameter on high latitude upper atmospheric humidity will be limited. The positive longwave feedback of emissivity in this study, as shown in Figure 9c and Figure S20 in Supporting Information S1, is instead related to the lower atmospheric humidity increase rather than changes in the upper atmosphere.

Cloud properties are also highly influenced by the parameters tuned in this study. From the zonal mean result, the cloud cover amount changes correspondingly with the relative humidity, which is mainly influenced by the surface temperature (Figure 12). Cloud coverage changes with the relative humidity in most latitudes, but is decoupled in the Southern Hemisphere high latitudes and the North Pole, where the relative humidity decreases

10.1029/2024PA004976

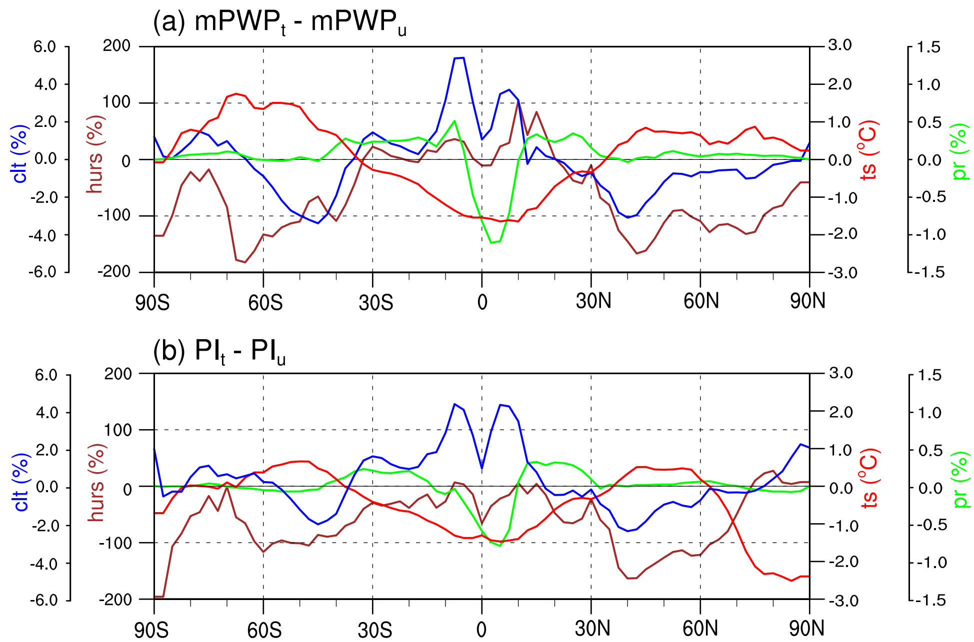

Figure 12. The zonal mean changes in cloud cover (CLT), relative humidity (HURS), TS and precipitation of the mPWP and the PI from HadCM3t compared to HadCM3u. (a): mPWP$_t$—mPWP$_u$; (b): PI$_t$—PI$_u$.

but cloud cover amount increases (Figure 12a and Figure S11 in Supporting Information S1). Over these regions the change in cloud coverage can be explained by other factors such as the tuned lower threshold of relative humidity for cloud formation. In other words, in regions that experience significant relative humidity change, any change of cloud coverage is dominated by the change of relative humidity which generates cloud, and these changes are the combined result of the tuned parameters; in regions with insignificant relative humidity change that are relatively dry, such as the high latitudes of both hemispheres, the changes in cloud can result from the reduced threshold of relative humidity for cloud formation which allows cloud to form in a relatively drier environment (Figure 12). There are other tuned parameters that change the cloud properties significantly. In this study, the cloud droplet number is decreased to 50 cm^{-3} and the cloud droplet radius is increased to 17 μm. Only consider the effects of model tuning, the combined influence of these two tuned parameter weakens cloud shortwave scattering significantly and therefore has a positive RE, and can be seen from changes in the cloud scattering induced RE (Figure S21 and S22 in Supporting Information S1). This is consistent with other paleoclimate simulations that have incorporated similar tuning to these two parameters, as well as with studies investigating aerosol-cloud interactions in paleoclimate background (e.g., Feng et al., 2019; Kiehl & Shields, 2013).

Changes in both cloud and atmospheric circulation will significantly affect precipitation. Spatially, precipitation generally increases where cloud coverage increases and vice versa. But this relationship is less obvious in the zonal average. By taking the atmospheric vertical movement into account, it can be seen that the precipitation anomaly is largely led by the changes in vertical air movement (Figure 4 and Figure S10 in Supporting Information S1). Moreover, the tuning of the model influenced the precipitation directly by increasing cloud droplet to rain conversion rate and decreasing the threshold of liquid water for the precipitation formation, as shown in Table 1. The effect after tuning these two parameters is to promote the conversion of cloud water droplets to rain (Rougier et al., 2009). Globally, the precipitation increases slightly by 0.03 mm/day, although global mean temperature and atmospheric humidity both decrease in the mPWP; in the PI, global mean temperature decreases more than the mPWP, and the global mean precipitation change is nearly 0.00 mm/day (Figure 12).

5. Conclusion

In this study, HadCM3t has been adopted to study the climate of mPWP. Compared with the previous version of HadCM3u, HadCM3t still performs well at simulating the preindustrial, but aligns with the reconstructed SSTAs much better due to a better represent of high latitudes warming.

Comparing to HadCM3u, HadCM3t simulated mPWP and PI show differences primarily in temperature, precipitation, atmospheric humidity, cloud, ice, and ocean circulation. After model tuning, from the perspective of the mPWP climatology anomalies relative to the PI: (a). The polar region becomes warmer, which leads the factor of polar warming to global warming from 2.0 of HadCM3u to 2.2 of HadCM3t; (b). The P-E change over the tropics becomes weaker; (c). The surface specific humidity increase becomes smaller over the tropics but larger over high latitudes; (d), the zonal averaged cloud coverage anomaly does not change significantly, but leads to a significant increase in the RE anomaly due to tuning on cloud drop number and cloud drop radii; (e). The ice concentration loss is larger; (f). The intensification of AMOC becomes stronger.

Compare the results of the same experiment run from HadCM3t and HadCM3u, after model tuning: (a). In the mPWP experiment, surface temperature increases significantly over the mid to high latitudes; in the PI experiment, surface temperature increases only over the mid-latitudes but decreases over the high latitudes; (b). For both the mPWP and PI, cloud increases over the low latitudes and high latitudes, but decreases over the mid-latitudes; (c). For both the mPWP and PI, precipitation decreases significantly near the equator but decreases over the rest regions of tropics and subtropics, in a global mean perspective, precipitation increases slightly by 0.03 mm/day, although global mean temperature decreases in the mPWP; (d). For both mPWP and PI, the global meridional overturning becomes more vigorous. For the same model parameters tuning, the PI and the mPWP has different response due to their different climate backgrounds and differences in their Earth's system.

To explore the difference in the responses between HadCM3t and HadCM3u simulated mPWP climates, the Earth system energy balance analysis and the further decomposition of shortwave flux are adopted by using EBM approach and APRP approach. The results show that, in terms of the mPWP temperature anomaly: (a). Compared to HadCM3u, the increased polar warming from HadCM3t are resulted from increased emissivity (0.6°C), decreased surface albedo (2.3 W/m^2 shortwave RE equals to 0.7°C warming) and changes in shortwave cloud (0.3 W/m^2 shortwave RE equals to 0.1°C warming); (b). In a global average perspective, changes in emissivity, surface albedo and shortwave cloud equally contribute 0.1°C warming to the difference in the temperature anomalies simulated by HadCM3t and HadCM3u. To summarize, after parameter tuning of HadCM3, the tuned HadCM3 performs as well as the original HadCM3 at simulating the preindustrial but aligns better with the reconstructed SSTAs of the mPWP mainly due to increased warmings from shortwave radiation change over high latitudes which are primarily from the surface albedo change. The change in emissivity contributes secondarily to the increased warming of the high latitudes. The change in cloud also makes positive contribution to the polar warming from both longwave and shortwave effects. By refining model parameters using past climate data, this study provides insights into improving the reliability of models to simulate future climates with similar conditions and feedback mechanisms.

Data Availability Statement

Climate Model data used in the study can be accessed at the repository of Bristol Research Initiative for the Dynamic Global Environment (BRIDGE) simulations data set https://www.paleo.bristol.ac.uk/ummodel/scripts/papers/Xin_et_al_2025.html. The data is analyzed with Python Version 3.11.5 and NCAR Command Language Version 6.6.2 (The NCAR Command Language, 2019).

Acknowledgments
This research is funded by the European Union's Horizon 2020 research and innovation programme under the Marie Skłodowska-Curie Grant agreement No 813360 4DREEF, and Natural Environment Research Council grant number NE/V01823X/1. This work was carried out using the computational facilities of the Advanced Computing Research Centre, University of Bristol—http://www.bris.ac.uk/acrc/.

References

Andrews, T., Forster, P. M., Boucher, O., Bellouin, N., & Jones, A. (2010). Precipitation, radiative forcing and global temperature change. *Geophysical Research Letters*, *37*(14). https://doi.org/10.1029/2010GL043991

Brady, E. C., Otto-Bliesner, B. L., Kay, J. E., & Rosenbloom, N. (2013). Sensitivity to glacial forcing in the CCSM4. *Journal of Climate*, *26*(6), 1901–1925. https://doi.org/10.1175/JCLI-D-11-00416.1

Bragg, F. J., Lunt, D. J., & Haywood, A. M. (2012). Mid-Pliocene climate modelled using the UK Hadley Centre Model: PlioMIP experiments 1 and 2. *Geoscientific Model Development*, *5*(5), 1109–1125. https://doi.org/10.5194/gmd-5-1109-2012

Brierley, C. M., Collins, M., & Thorpe, A. J. (2010). The impact of perturbations to ocean-model parameters on climate and climate change in a coupled model. *Climate Dynamics*, *34*(2), 325–343. https://doi.org/10.1007/s00382-008-0486-3

Chandan, D., & Peltier, W. R. (2018). On the mechanisms of warming the mid-Pliocene and the inference of a hierarchy of climate sensitivities with relevance to the understanding of climate futures. *Climate of the Past*, *14*(6), 825–856. https://doi.org/10.5194/cp-14-825-2018

Collins, M., Brierley, C. M., MacVean, M., Booth, B. B. B., & Harris, G. R. (2007). The sensitivity of the rate of transient climate change to ocean physics perturbations. *Journal of Climate*, *20*(10), 2315–2320. https://doi.org/10.1175/JCLI4116.1

Cox, P. M., Betts, R. A., Bunton, C. B., Essery, R. L., Rowntree, P. R., & Smith, J. (1999). The impact of new land surface physics on the GCM simulation of climate and climate sensitivity. *Climate Dynamics*, *15*, 183–203. https://doi.org/10.1007/S003820050276/METRICS

Dolan, A. M., de Boer, B., Bernales, J., Hill, D. J., & Haywood, A. M. (2018). High climate model dependency of Pliocene Antarctic ice-sheet predictions. *Nature Communications*, *9*(1), 2799. https://doi.org/10.1038/s41467-018-05179-4

Dowsett, H., Dolan, A., Rowley, D., Moucha, R., Forte, A. M., Mitrovica, J. X., et al. (2016). The PRISM4 (Mid-Piacenzian) paleoenvironmental reconstruction. *Climate of the Past*, *12*(7), 1519–1538. https://doi.org/10.5194/cp-12-1519-2016

Essery, R., Best, M., & Cox, P. (2001). *Moses 2.2 technical documentation (Tech. Rep. No. HCTN 030)* (p. 31). Met Office Hadley Centre. Retrieved from https://library.metoffice.gov.uk/Portal/Default/en-GB/DownloadImageFile.ashx?objectId=1038&ownerType=0&ownerId=252314(Report,electronic

Feng, R., Otto-Bliesner, B. L., Fletcher, T. L., Tabor, C. R., Ballantyne, A. P., & Brady, E. C. (2017). Amplified late Pliocene terrestrial warmth in northern high latitudes from greater radiative forcing and closed Arctic Ocean gateways. *Earth and Planetary Science Letters*, *466*, 129–138. https://doi.org/10.1016/j.epsl.2017.03.006

Feng, R., Otto-Bliesner, B. L., Xu, Y., Brady, E., Fletcher, T., & Ballantyne, A. (2019). Contributions of aerosol-cloud interactions to Mid-Piacenzian seasonally sea ice-free Arctic Ocean. *Geophysical Research Letters*, *46*(16), 9920–9929. https://doi.org/10.1029/2019GL083960

Frieler, K., Meinshausen, M., Schneider von Deimling, T., Andrews, T., & Forster, P. (2011). Changes in global-mean precipitation in response to warming, greenhouse gas forcing and black carbon. *Geophysical Research Letters*, *38*(4). https://doi.org/10.1029/2010GL045953

Gordon, C., Cooper, C., Senior, C. A., Banks, H., Gregory, J. M., Johns, T. C., et al. (2000). The simulation of SST, sea ice extents and ocean heat transports in a version of the Hadley Centre Coupled Model without flux adjustments. *Climate Dynamics*, *16*(2), 147–168. https://doi.org/10.1007/S003820050010

Gregoire, L. J., Valdes, P. J., Payne, A. J., & Kahana, R. (2011). Optimal tuning of a GCM using modern and glacial constraints. *Climate Dynamics*, *37*, 705–719. https://doi.org/10.1007/S00382-010-0934-8/FIGURES/13

Gregory, J. M., Church, J. A., Boer, G. J., Dixon, K. W., Flato, G. M., Jackett, D. R., et al. (2001). Comparison of results from several AOGCMs for global and regional sea-level change 1900-2100. *Climate Dynamics*, *18*(3–4), 223–240. https://doi.org/10.1007/S003820100180/METRICS

Gregory, J. M., Ingram, W. J., Palmer, M. A., Jones, G. S., Stott, P. A., Thorpe, R. B., et al. (2004). A new method for diagnosing radiative forcing and climate sensitivity. *Geophysical Research Letters*, *31*(3). https://doi.org/10.1029/2003GL018747

Haywood, A. M., Dowsett, H. J., Dolan, A. M., Rowley, D., Abe-Ouchi, A., Otto-Bliesner, B., et al. (2016). The Pliocene model Intercomparison Project (PlioMIP) phase 2: Scientific objectives and experimental design. *Climate of the Past*, *12*(3), 663–675. https://doi.org/10.5194/cp-12-663-2016

Haywood, A. M., Hill, D. J., Dolan, A. M., Otto-Bliesner, B. L., Bragg, F., Chan, W. L., et al. (2013). Large-scale features of Pliocene climate: Results from the Pliocene model intercomparison project. *Climate of the Past*, *9*(1), 191–209. https://doi.org/10.5194/cp-9-191-2013

Haywood, A. M., Tindall, J. C., Burton, L. E., Chandler, M. A., Dolan, A. M., Dowsett, H. J., et al. (2024). Pliocene model intercomparison project phase 3 (Pliomip3) – Science plan and experimental design. *Global and Planetary Change*, *232*, 104316. https://doi.org/10.1016/j.gloplacha.2023.104316

Haywood, A. M., Tindall, J. C., Dowsett, H. J., Dolan, A. M., Foley, K. M., Hunter, S. J., et al. (2020). The Pliocene Model intercomparison project phase 2: Large-scale climate features and climate sensitivity. *Climate of the Past*, *16*(6), 2095–2123. https://doi.org/10.5194/cp-16-2095-2020

Heinemann, M., Jungclaus, J. H., & Marotzke, J. (2009). Warm Paleocene/Eocene climate as simulated in ECHAM5/MPI-OM. *Climate of the Past*, *5*(4), 785–802. https://doi.org/10.5194/cp-5-785-2009

Hill, D. J. (2015). The non-analogue nature of Pliocene temperature gradients. *Earth and Planetary Science Letters*, *425*, 232–241. https://doi.org/10.1016/j.epsl.2015.05.044

Hill, D. J., Haywood, A. M., Lunt, D. J., Hunter, S. J., Bragg, F. J., Contoux, C., et al. (2014). Evaluating the dominant components of warming in Pliocene climate simulations. *Climate of the Past*, *10*(1), 79–90. https://doi.org/10.5194/CP-10-79-2014

Houghton, J. T., Ding, Y., Griggs, D. J., Noguer, M., van der Linden, P. J., & Dai, X. (2001). IPCC, 2001: Climate change 2001: The scientific basis. Contribution of working group I to the third assessment report of the intergovernmental panel on climate change. *Cambridge University Press*, *881pp*(9).

Hourdin, F., Mauritsen, T., Gettelman, A., Golaz, J. C., Balaji, V., Duan, Q., et al. (2017). The art and science of climate model tuning. *Bulletin of the American Meteorological Society*, *98*, 589–602. https://doi.org/10.1175/BAMS-D-15-00135.1

Howell, F. W., Haywood, A. M., Dolan, A. M., Dowsett, H. J., Francis, J. E., Hill, D. J., et al. (2014). Can uncertainties in sea ice albedo reconcile patterns of data-model discord for the Pliocene and 20th/21st centuries? *Geophysical Research Letters*, *41*(6), 2011–2018. https://doi.org/10.1002/2013GL058872

Howell, F. W., Haywood, A. M., Dowsett, H. J., & Pickering, S. J. (2016). Sensitivity of Pliocene Arctic climate to orbital forcing, atmospheric CO_2 and sea ice albedo parameterisation. *Earth and Planetary Science Letters*, *441*, 133–142. https://doi.org/10.1016/j.epsl.2016.02.036

Huang, B., Thorne, P. W., Banzon, V. F., Boyer, T., Chepurin, G., Lawrimore, J. H., et al. (2017). Extended Reconstructed Sea Surface Temperature, Version 5 (ERSSTV5): Upgrades, validations, and intercomparisons. *Journal of Climate*, *30*(20), 8179–8205. https://doi.org/10.1175/JCLI-D-16-0836.1

Hunter, S. J., Haywood, A. M., Dolan, A. M., & Tindall, J. C. (2019). The HadCM3 contribution to PlioMIP phase 2. *Climate of the Past*, *15*(5), 1691–1713. https://doi.org/10.5194/cp-15-1691-2019

Irvine, P. J., Gregoire, L. J., Lunt, D. J., & Valdes, P. J. (2013). An efficient method to generate a perturbed parameter ensemble of a fully coupled AOGCM without flux-adjustment. *Geoscientific Model Development*, *6*(5), 1447–1462. https://doi.org/10.5194/gmd-6-1447-2013

Johns, T. C., Carnell, R. E., Crossley, J. F., Gregory, J. M., Mitchell, J. F., Senior, C. A., et al. (1997). The second Hadley Centre coupled ocean-atmosphere GCM: Model description, Spinup and validation. *Climate Dynamics*, *13*(2), 103–134. https://doi.org/10.1007/s003820050155

Kageyama, M., Harrison, S. P., Kapsch, M.-L., Lofverstrom, M., Lora, J. M., Mikolajewicz, U., et al. (2021). The PMIP4 last glacial maximum experiments: Preliminary results and comparison with the PMIP3 simulations. *Climate of the Past*, *17*(3), 1065–1089. https://doi.org/10.5194/cp-17-1065-2021

Kiehl, J. T., & Shields, C. A. (2013). Sensitivity of the Palaeocene-Eocene thermal maximum climate to cloud properties. *Philosophical Transactions of the Royal Society A: Mathematical, Physical & Engineering Sciences*, *371*(2001), 20130093. https://doi.org/10.1098/rsta.2013.0093

Lohmann, G., Knorr, G., Hossain, A., & Stepanek, C. (2022). Effects of CO_2 and ocean mixing on Miocene and Pliocene temperature gradients. *Paleoceanography and Paleoclimatology*, *37*(2), e2020PA003953. https://doi.org/10.1029/2020PA003953

Lunt, D. J., Bragg, F., Chan, W.-L., Hutchinson, D. K., Ladant, J.-B., Morozova, P., et al. (2021). DeepMIP: Model intercomparison of early Eocene Climatic Optimum (EECO) large-scale climate features and comparison with proxy data. *Climate of the Past*, *17*(1), 203–227. https://doi.org/10.5194/cp-17-203-2021

Lunt, D. J., Dunkley Jones, T., Heinemann, M., Huber, M., LeGrande, A., Winguth, A., et al. (2012). A model–data comparison for a multi-model ensemble of early Eocene atmosphere–ocean simulations: EoMIP. *Climate of the Past*, *8*(5), 1717–1736. https://doi.org/10.5194/cp-8-1717-2012

McClymont, E. L., Ford, H. L., Ho, S. L., Tindall, J. C., Haywood, A. M., Alonso-Garcia, M., et al. (2020). Lessons from a high CO_2 world: An ocean view from 3 million years ago. *Climate of the Past*, *16*(4), 1599–1615. https://doi.org/10.5194/cp-16-1599-2020

McClymont, E. L., Ho, S. L., Ford, H. L., Bailey, I., Berke, M. A., Bolton, C. T., et al. (2023). Synthesis of sea surface temperature and foraminifera stable isotope data spanning the Mid-Pliocene warm period and early Pleistocene (PlioVAR) [Dataset]. *PANGAEA*. https://doi.org/10.1594/PANGAEA.956158

Mitchell, D. L., Mishra, S., & Lawson, R. P. (2011). Representing the ice fall speed in climate models: Results from tropical composition, cloud and climate coupling (TC4) and the Indirect and Semi-Direct Aerosol Campaign (ISDAC). *Journal of Geophysical Research*, *116*(0–03), D00T03. https://doi.org/10.1029/2010JD015433

Mulholland, D. P., Haines, K., Sparrow, S. N., & Wallom, D. (2017). Climate model forecast biases assessed with a perturbed physics ensemble. *Climate Dynamics*, *49*, 1729–1746. https://doi.org/10.1007/S00382-016-3407-X/FIGURES/9

Murphy, J., Sexton, D., Jenkins, G., Boorman, P., Booth, B., Brown, C., et al. (2009). UK climate projections science report. *Climate change projections*.

Murphy, J. M., Sexton, D. M., Barnett, D. H., Jones, G. S., Webb, M. J., Collins, M., & Stainforth, D. A. (2004). Quantification of modelling uncertainties in a large ensemble of climate change simulations. *Nature*, *430*(7001), 768–772. https://doi.org/10.1038/nature02771

Peatier, S., Sanderson, B. M., Terray, L., & Roehrig, R. (2022). Investigating parametric dependence of climate feedbacks in the atmospheric component of CNRM-CM6-1. *Geophysical Research Letters*, *49*(9), e2021GL095084. https://doi.org/10.1029/2021GL095084

Pope, V. D., Gallani, M. L., Rowntree, P. R., & Stratton, R. A. (2000). The impact of new physical parametrizations in the Hadley Centre climate model: HadAM3. *Climate Dynamics*, *16*(2), 123–146. https://doi.org/10.1007/S003820050009

Ramanathan, V., Crutzen, P. J., Kiehl, J. T., & Rosenfeld, D. (2001). Aerosols, climate, and the hydrological cycle. *Science*, *294*(5549), 2119–2124. https://doi.org/10.1126/science.1064034

Ren, X., Lunt, D. J., Hendy, E., von der Heydt, A., Abe-Ouchi, A., Otto-Bliesner, B., et al. (2023). The hydrological cycle and ocean circulation of the Maritime continent in the Pliocene: Results from PlioMIP2. *Climate of the Past*, *19*(10), 2053–2077. https://doi.org/10.5194/cp-19-2053-2023

Roach, L. A., Tett, S. F., Mineter, M. J., Yamazaki, K., & Rae, C. D. (2018). Automated parameter tuning applied to sea ice in a global climate model. *Climate Dynamics*, *50*, 51–65. https://doi.org/10.1007/S00382-017-3581-5/TABLES/3

Ross, P. I. (2023). *Deep ocean circulation during the early Eocene: A model-data comparison*. [Doctoral Dissertation, Thesis]. University College London.

Rougier, J., Sexton, D. M., Murphy, J. M., & Stainforth, D. (2009). Analyzing the climate sensitivity of the HadSM3 climate model using ensembles from different but related experiments. *Journal of Climate*, *22*(13), 3540–3557. https://doi.org/10.1175/2008JCLI2533.1

Sagoo, N., Valdes, P., Flecker, R., & Gregoire, L. J. (2013). The Early Eocene equable climate problem: Can perturbations of climate model parameters identify possible solutions? *Philosophical Transactions of the Royal Society A: Mathematical, Physical & Engineering Sciences*, *371*(2001), 20130123. https://doi.org/10.1098/rsta.2013.0123

Sanderson, B. M. (2011). A multimodel study of parametric uncertainty in predictions of climate response to rising greenhouse gas concentrations. *Journal of Climate*, *24*(5), 1362–1377. https://doi.org/10.1175/2010JCLI3498.1

Sanderson, B. M., Piani, C., Ingram, W. J., Stone, D. A., & Allen, M. R. (2008). Towards constraining climate sensitivity by linear analysis of feedback patterns in thousands of perturbed-physics GCM simulations. *Climate Dynamics*, *30*(2–3), 175–190. https://doi.org/10.1007/s00382-007-0280-7

Sanderson, B. M., & Shell, K. M. (2012). Model-specific radiative kernels for calculating cloud and noncloud climate feedbacks. *Journal of Climate*, *25*(21), 7607–7624. https://doi.org/10.1175/JCLI-D-11-00726.1

Sexton, D. M., McSweeney, C. F., Rostron, J. W., Yamazaki, K., Booth, B. B., Murphy, J. M., et al. (2021). A perturbed parameter ensemble of hadgem3-gc3.05 coupled model projections: Part 1: Selecting the parameter combinations. *Climate Dynamics*, *56*(11–12), 3395–3436. https://doi.org/10.1007/s00382-021-05709-9

Shiogama, H., Watanabe, M., Ogura, T., Yokohata, T., & Kimoto, M. (2014). Multi-Parameter Multi-Physics Ensemble (MPMPE): A new approach exploring the uncertainties of climate sensitivity. *Atmospheric Science Letters*, *15*(2), 97–102. https://doi.org/10.1002/asl2.472

Shiogama, H., Watanabe, M., Yoshimori, M., Yokohata, T., Ogura, T., Annan, J. D., et al. (2012). Perturbed physics ensemble using the miroc5 coupled atmosphere-ocean GCM without flux corrections: Experimental design and results: Parametric uncertainty of climate sensitivity. *Climate Dynamics*, *39*(12), 3041–3056. https://doi.org/10.1007/S00382-012-1441-X/FIGURES/14

Slivinski, L. C., Compo, G. P., Whitaker, J. S., Sardeshmukh, P. D., Giese, B. S., McColl, C., et al. (2019). Towards a more reliable historical reanalysis: Improvements for version 3 of the twentieth century reanalysis system. *Quarterly Journal of the Royal Meteorological Society*, *145*(724), 2876–2908. https://doi.org/10.1002/QJ.3598

Smith, D. M., Cusack, S., Colman, A. W., Folland, C. K., Harris, G. R., & Murphy, J. M. (2007). Improved surface temperature prediction for the coming decade from a global climate model. *Science*, *317*(5839), 796–799. https://doi.org/10.1126/science.1139540

Smith, D. M., Screen, J. A., Deser, C., Cohen, J., Fyfe, J. C., García-Serrano, J., et al. (2019). The Polar Amplification Model Intercomparison Project (PAMIP) contribution to CMIP6: Investigating the causes and consequences of polar amplification. *Geoscientific Model Development*, *12*(3), 1139–1164. https://doi.org/10.5194/gmd-12-1139-2019

Solomon, S., Qin, D., Manning, M., Chen, Z., Marquis, M., Averyt, K., et al. (2007). *IPCC, 2007: Climate change 2007: The physical science basis. Contribution of working group I to the Fourth assessment report of the intergovernmental panel on climate change*. In (p. 996). Cambridge University Press, . Retrieved from https://www.ipcc.ch/report/ar4/wg1/

Taylor, K. E., Crucifix, M., Braconnot, P., Hewitt, C. D., Doutriaux, C., Broccoli, A. J., et al. (2007). Estimating shortwave radiative forcing and response in climate models. *Journal of Climate*, *20*(11), 2530–2543. https://doi.org/10.1175/JCLI4143.1

The NCAR Command Language. (2019). The NCAR Command Language (version 6.6.2) [Software]. *UCAR/NCAR/CISL/TDD*. https://doi.org/10.5065/D6WD3XH5

Tindall, J. C., & Haywood, A. M. (2020). Modelling the mid-Pliocene warm period using HadGEM2. *Global and Planetary Change*, *186*, 103110. https://doi.org/10.1016/j.gloplacha.2019.103110

10.1029/2024PA004976

Tindall, J. C., Haywood, A. M., Salzmann, U., Dolan, A. M., & Fletcher, T. (2022). The warm winter paradox in the Pliocene northern high latitudes. *Climate of the Past*, *18*(6), 1385–1405. https://doi.org/10.5194/cp-18-1385-2022

Valdes, P. J., Armstrong, E., Badger, M. P. S., Bradshaw, C. D., Bragg, F., Crucifix, M., et al. (2017). The BRIDGE HadCM3 family of climate models: HadCM3@Bristol v1.0. Geosci. *Model Dev*, *10*, 3715–3743. https://doi.org/10.5194/gmd-10-3715-2017

Wetherald, R. T., & Manabe, S. (1988). Cloud feedback processes in a general circulation model. *Journal of the Atmospheric Sciences*, *45*(8), 1397–1415. https://doi.org/10.1175/1520-0469(1988)045⟨1397:cfpiag⟩2.0.co;2

Williams, C. J. R., Sellar, A. A., Ren, X., Haywood, A. M., Hopcroft, P., Hunter, S. J., et al. (2021). Simulation of the Mid-Pliocene warm period using HadGEM3: Experimental design and results from model–model and model–data comparison. *Climate of the Past*, *17*(5), 2139–2163. https://doi.org/10.5194/cp-17-2139-2021

Yamazaki, K., Sexton, D. M. H., Rostron, J. W., McSweeney, C. F., Murphy, J. M., & Harris, G. R. (2021). A perturbed parameter ensemble of hadgem3-gc3.05 coupled model projections: Part 2: Global performance and future changes. *Climate Dynamics*, *56*(11–12), 3437–3471. https://doi.org/10.1007/s00382-020-05608-5

Zelinka, M. D., Smith, C. J., Qin, Y., & Taylor, K. E. (2023). Comparison of methods to estimate aerosol effective radiative forcings in climate models. *Atmospheric Chemistry and Physics*, *23*(15), 8879–8898. https://doi.org/10.5194/acp-23-8879-2023

Zhu, J., Poulsen, C. J., & Tierney, J. E. (2019). Simulation of Eocene extreme warmth and high climate sensitivity through cloud feedbacks (pp. 1–10).